science.sciencemag.org/content/364/6441/658/suppl/DC1

Supplementary Materials for

De novo design of tunable, pH-driven conformational transitions

Scott E. Boyken, Mark A. Benhaim, Florian Busch, Mengxuan Jia, Matthew J. Bick, Heejun Choi, Jason C. Klima, Zibo Chen, Carl Walkey, Alexander Mileant, Aniruddha Sahasrabuddhe, Kathy Y. Wei, Edgar A. Hodge, Sarah Byron, Alfredo Quijano-Rubio, Banumathi Sankaran, Neil P. King, Jennifer Lippincott-Schwartz, Vicki H. Wysocki, Kelly K. Lee, David Baker*

*Corresponding author. Email: dabaker@uw.edu

Published 17 May 2019, *Science* **364**, 658 (2019)

This PDF file includes:

Supplementary Text

Modeling the pH-dependence and free energies of assembly

Modeling the pH-dependence of assembly.

Modeling the pH-dependence of unfolding of a protein with N interacting ionizable residues in the general case requires computing the partition function over all 2^N distinct combinations of protonation states in both the folded and unfolded states, including the appropriate ionization-state dependent electrostatic interaction terms (eq. 1-8 of ref. *39*). Given the challenge in accurately computing these interaction terms, and the complexity of the full native state partition function, it is not straightforward to use this model to guide the tuning of the pH-dependence and in interpreting the experimental data. Hence it is useful to consider the considerably simpler expression that describes the limiting case, in which all N sites are assumed to be identical, and do not become protonated in the native state; this collapses the partition function for the native state ensemble to one term (where all sites are deprotonated), and the unfolded state partition function can be readily evaluated assuming all sites are independent. In the case of *m* histidine sites, which when exposed to solvent have a pKa of ~6.0, the resultant expression is

$$\textbf{(Eq. S1)} \quad \Delta G_{fold} = \Delta G_{fold_{neutral}} - R \cdot T \cdot m \cdot ln\,(1 + e^{-\ln(10)\cdot(pH-6.0)}) \tag{S1}$$

where ΔG_{fold} is the free energy of unfolding, $\Delta G_{fold_{neutral}}$ is the free energy of unfolding at neutral pH, R is the gas constant, and T is temperature. For simplicity, we consider only the equilibrium between folded trimer and unfolded monomers; we do not consider partially folded monomeric states or attempt to model the equilibria with the higher order species observed by

mass spectrometry as this would introduce many new parameters. To evaluate the validity of this approximation for describing the pH-dependence of the free energy for the designs in this paper, we selected design pRO-2.3 (Figure 2A), which has a relatively low unfolding pH of approximately 4.5 (Figure 3D, Table S3), and mapped the pH-dependence of unfolding over a broad pH range by combining estimates of the free energy of unfolding from (1) direct measurements of the population fraction of trimer from native mass spectrometry experiments in the pH-unfolding transition region (pH 4.0-5.0), and (2) guanidine denaturation experiments in the folded regime (pH 5.0-7.0) (Fig. S15). The free energy of folding decreases moderately from pH 7.0 to pH 6.0, and then decreases steeply to become negative below pH 4.5. Fitting to Eq. S1 yields an estimate of 7.3 ± 0.3 kcal/mol for the free energy of unfolding at pH 6.0 and 3.5 ± 0.1 for the number of histidine sites protonated. While the assumption that none of the histidines can be protonated in the folded state at any pH is clearly an oversimplification, 3.5 is within a factor of two of the actual number of sites (6 histidine residues in design pRO-2.3), and the overall fit to the data is reasonable given only two free parameters (m and $\Delta G_{fold_{neutral}}$). Thus, with the proviso that the model is clearly an oversimplification, we use it to guide the qualitative tuning of the pH-dependence of unfolding as described in the following section and the main text.

Modeling free energy of assembly of trimer designs with variable numbers of hydrophobic, polar, and histidine containing layers.

To adapt Eq. S1 to qualitatively model the pH-dependence of the free energy of assembly for a homotrimer with *n* pH-independent hydrophobic layers, *m* pH-dependent hydrogen bond network layers each containing three histidine residues, and *l* hydrogen bond network layers

lacking histidine, we split the free energy of folding (assembly) at neutral pH into contributions from the three types of layers, yielding

$$\textbf{(Eq. S2)} \quad \%\, trimer \; = \frac{100}{1+e^{-\frac{1}{RT}\left[\Delta G_{assembly}\right]}}$$

$$\Delta G_{assembly} = n \cdot \Delta G_{hydrophobic} + m \cdot \Delta G_{polar_m} + l \cdot \Delta G_{polar_l} - 3m \cdot RT \cdot \ln(1 \; + \; e^{-\ln(10)\cdot(pH-6.0)})$$

where $\Delta G_{hydrophobic}$, ΔG_{polar_m}, and ΔG_{polar_l} are the free energies of formation of hydrophobic layers, pH-responsive polar layers, and pH-independent polar layers, respectively; R is the gas constant; T is temperature; the change in pH is relative to the pKa of solvent-exposed histidine (~6.0), and the midpoint of the transition of disassembly (pH set point) is the pH at which the free energy of assembly (quantity in square brackets) is zero. Estimates of $\Delta G_{hydrophobic}$, ΔG_{polar_m}, and ΔG_{polar_l} were obtained from guanidine denaturation experiments (Figure 3B) as follows:

Because we know the estimated free energy of folding for each design (Figure 3B and fig. S6), and we also know the number of n, m, and l layer types for each design, we can solve a system of linear equations to estimate the free energy of formation of each individual layer type: $\Delta G_{hydrophobic}$ for n, ΔG_{polar_m} for m, and ΔG_{polar_l} for l. For example, design pRO-2 has a free energy of folding of 8.1 kcal/mol (fig. S6) and has 6n, 3m, and 0l layers; design pRO-2.1 has a free energy of folding of 13.5 kcal/mol (fig. S6) and has 7n, 2m, and 0l layers; design pRO-2-noHis has a free energy of folding of 6.1 kcal/mol (fig. S6) and has 6n, 0m, and 3l layers. Solving these equations yields estimates of the free energy contribution of each layer type, which are used in subsequent calculations:

$\Delta G_{hydrophobic}$= 2.7 kcal/mol, ΔG_{polar_m}= -2.8 kcal/mol, and ΔG_{polar_l}= -3.41 kcal/mol

Extracting transition cooperativity and pH midpoint from native mass spectrometry data

We fit the experimental native mass spectrometry data to a simple sigmoid model that assumes that the starting point is 100% trimer and the endpoint is 0% trimer:

$$\textbf{(Eq. S3)} \quad \%\, trimer \; = \frac{100}{1+e^{-k(pH-pH_0)}}$$

where k is the cooperativity of the transition and pH_0 is the transition pH (midpoint of trimer dissociation). We can then compare the values of k and pH_0 for each design to those predicted by Equation S2 given the number of hydrophobic (n), polar (l) and histidine network (m) layers. As is evident from table S3, while there is overall qualitative agreement, the model is clearly far from perfect; the inaccuracies likely stem from both the considerable simplifications leading to Eq. S1 as well as the context-dependent effects described in the main text. Overall trends are correctly recapitulated by the model; for example, the dependence of pH_0 on the ratio of m/n (Figure 3E), and all designs tested have predicted pH_0 values that are within ~0.5 pH units of experimentally observed values (table S3). Because pH_0 is the pH at which the free energy of assembly is zero, we can relate Eq. S2 and Eq. S3 as follows to predict the cooperativity (k) and pH transition point (pH_0) as functions of n, m, and l.

The transition pH (pH_0) is the pH at which the free energy of assembly ($\Delta G_{assembly}$) is zero:

$$0 = n \cdot \Delta G_{hydrophobic} + m \cdot \Delta G_{polar_m} + l \cdot \Delta G_{polar_l} - \; 3m \cdot R \cdot T \cdot \ln(1 \; + \; e^{-\ln(10) \cdot (pH_0 - 6.0)})$$

Rearranging:

$$3m \cdot R \cdot T \cdot \ln(1 \; + \; e^{-\ln(10) \cdot (pH_0 - 6.0)}) = n \cdot \Delta G_{hydrophobic} + m \cdot \Delta G_{polar_m} + l \cdot \Delta G_{polar_l}$$

$$3m \cdot \ln(1 + e^{-\ln(10)\cdot(pH_0-6.0)}) = \frac{n \cdot \Delta G_{hydrophobic} + m \cdot \Delta G_{polar_m} + l \cdot \Delta G_{polar_l}}{R \cdot T}$$

Assume $\ln(1 + e^{-\ln(10)\cdot(pH_0-6.0)})$ is approximately $\ln(e^{-\ln(10)\cdot(pH_0-6.0)})$:

$$-3 \cdot m \cdot \ln(10) \cdot (pH_0 - 6.0) = \frac{n \cdot \Delta G_{hydrophobic} + m \cdot \Delta G_{polar_m} + l \cdot \Delta G_{polar_l}}{R \cdot T}$$

Comparing to Eq. S3, we can deduce that *k* is approximately $3m \cdot \ln(10)$, giving us a way to predict *k* as a function of *n*, *m*, *l*. Further rearrangement of the equations to isolate pH_0 gives us a way to predict the transition pH as a function of *n*, *m*, *l*:

(Eq. S4) $$pH_0 = 6.0 - \left[\frac{n\cdot\Delta G_{hydrophobic} + m\cdot\Delta G_{polar_m} + l\cdot\Delta G_{polar_l}}{3\cdot m\cdot\ln(10)\cdot R\cdot T}\right]$$

Collectively, these equations give us a framework to understand our experimental results and make predictions to qualitatively tune the pH set point and cooperativity in our designed pH-responsive oligomers (pRO's).

Another common measure of cooperativity is the Hill coefficient, which has been used in the studies of the pH-dependence of protein folding and stability(*40*, *41*); in our system, it can be estimated as

(Eq. S5) $$\%\, trimer = \frac{100}{1+10^{-n_h\cdot(pH - pH_0)}}$$

where n_h is the Hill coefficient.

For circular dichroism guanidine denaturation experiments in which the mean residue ellipticity at 222 nm (MRE_{222nm}) is measured versus guanidinium chloride concentration ($[GdmCl]$), the free energy of unfolding ΔG_{fold}, the dependence of ΔG_{fold} on guanidinium chloride

concentration m_{GdmCl}, and fitting parameters B,C, and D can be approximated by the following expression, where R is the gas constant and T is temperature:

$$\textbf{(Eq. S6)} \quad MRE_{222nm} = B + \frac{C\cdot(1+(D\cdot[GdmCl]))}{1+e^{-\frac{1}{R\cdot T}\left(\Delta G_{fold}-(m_{GdmCl}\cdot[GdmCl])\right)}}$$

For native mass spectrometry experiments, the free energy of unfoldingΔG_{fold}can be approximated from the measured population percent of trimer by the expression:

$$\textbf{(Eq. S7)} \quad \Delta G_{fold} = R\cdot T\cdot \ln\left(\frac{1}{\frac{100}{(\%\ trimer)}-1}\right)$$

Materials and Methods

Computational Design Methods

Backbone sampling: Oligomeric protein backbones with an inner and outer ring of α-helices were produced by systematically varying helical parameters using the Crick generating equations(*18*, *19*). Ideal values were used for the supercoil twist (ω_0) and helical twist (ω_1)(*18*, *19*). Starting points for the superhelical radii were chosen based on successful previous designs(*20*) and the helical phase ($\Delta\phi_1$) was sampled from 0° to 90° with a step size of 10°. The offset along the z-axis (Z-offset) for the first helix was fixed to 0 as a reference point, with the rest of the helices independently sampled from -1.51 Å to 1.51 Å, with a step size of 1.51 Å. For heterodimer designs, supercoil phases ($\Delta\phi_0$) were fixed at 0°, 90°, 180° and 270°, respectively, for the four helices. The inner and outer helices were connected by short,

structured loops as described previously(*20*). To find backbones that could accommodate more than two histidine networks, a second round of parametric design was performed with finer sampling around the helical parameters of the initial designs. (*Note*: because the inner and outer helices have different superhelical radii, the repeating geometric cross sections of the helical bundle are not always perfect geometric repeats along the z-axis; hence, because of the geometric sensitivity of hydrogen bonding, finer sampling was required to find backbones that could accommodate the same histidine hydrogen bond networks at multiple layers / cross sections).

Design of histidine networks: the HBNet(*20*) method in Rosetta(*22*) was extended to include program code that allowed for the selection of hydrogen bond networks that contain at least one histidine at oligomeric interfaces, and also the option to select for cases where the histidine residue accepts a hydrogen bond across the oligomeric interface. HBNet was used to select backbones that could accommodate 1-4 such networks in the homotrimeric and heterodimeric backbones.

Rosetta design calculations: To design the sequence and sidechain rotamer conformations for the rest of the protein surrounding the hydrogen bond networks, the network residues were constrained using AtomPair constraints on the donors and acceptors of the hydrogen bonds and RosettaDesign calculations carried out, and best designs selected, as described previously(*20*).

Design strategy to tune pH set point and cooperativity via modular placement of the histidine networks: Once successful designs were identified, HBNet was used to generate all possible

combinations of hydrogen bond network placement for the existing networks within the backbone of that design; for each, the amino acid sequence and side chain rotamer conformations were optimized around those placed networks as described above. From these combinations for pRO-2, designs pRO-2.1-2.5 (Figure 3) were selected based on placement of networks *m* and *l* relative to the hydrophobic layers, *n*, to test our tuning strategy. Design pRO-2 mutants I56V and A54M were designed rationally without any computational design.

Rosetta design scripts are available in the following github repository: https://github.com/sboyken/pHresponsiveOligomers

New program code for designing pH-responsive networks in HBNet is written in C++ as part of the Rosetta software suite: (https://www.rosettacommons.org/software).

Protein expression and purification

Plasmids containing synthetic genes that encode the designed proteins were ordered through Genscript Inc. (Piscataway, N.J., USA), cloned into the NdeI and XhoI sites of either pET21-NESG or pET-28b vectors (see table S1). Plasmids were transformed into chemically competent *E. coli* expression strains BL21(DE3)Star (Invitrogen) or Lemo21(DE3) (New England Biolabs). Following transformation, single colonies were picked from agar plates and grown overnight in 5 ml starter cultures of Luria-Bertani (LB) medium containing 50 μg/mL carbenicillin (for pET21-NESG vectors) or kanamycin (for pET-28b vectors) with shaking at 225 rpm for 12-18 hours at 37°C. 5 ml starter cultures were added to 500 ml TBM-5052 with antibiotic for expression by autoinduction(*42*); cells were grown at 37°C for 4-7 hours and temperature was dropped to 18°C

overnight. After 18-24 hours, cells were harvested by centrifugation for 15 minutes at 5000 rcf at 4°C and resuspended in 20 ml lysis buffer (25 mM Tris pH 8.0 at room temperature, 300 mM NaCl, 20 mM Imidazole).

Cells were lysed by microfluidization in the presence of 1 mM PMSF. Lysates were clarified by centrifugation at 24,000 rcf at 4°C for at least 30 minutes. Proteins were purified by Immobilized metal affinity chromatography (IMAC): supernatant was applied to Ni-NTA (Qiagen) columns pre-equilibrated in lysis buffer. The column was washed twice with 15 column volumes (CV) of wash buffer (25 mM Tris pH 8.0 at room temperature, 300 mM NaCl, 40 mM Imidazole), followed by 3-5 CV of high-salt wash buffer (25 mM Tris pH 8.0 at room temperature, 1 M NaCl, 40 mM Imidazole) then an additional 15 CV of wash buffer. Protein was eluted with 250 mM Imidazole, and buffer-exchanged into 25 mM Tris pH 8.0 and 150 mM NaCl without imidazole for cleavage of the N-terminal hexahistidine tag by purified hexahistidine-tagged TEV protease (with the exception of design pRO-1, which was cleaved using restriction grade thrombin (EMD Millipore 69671-3) at room temperature for 4 hours or overnight, using a 1:5000 dilution of enzyme into sample solution). A second Ni-NTA step was used to remove hexahistidine tag, uncleaved sample and the hexahistidine-tagged TEV protease, and the cleaved proteins were then concentrated and further purified by gel filtration using FPLC and a Superdex^{TM} 75 Increase 10/300 GL (GE) size exclusion column in 25 mM Tris pH 8.0 at room temperature, 150 mM NaCl, and 2% glycerol.

Buffers for varying pH

For low-pH experiments involving circular dichroism (CD), small-angle X-ray scattering (SAXS), and size exclusion chromatography (SEC), Na_2HPO_4-Citrate buffer was used to ensure

that a single buffer system could be used that was stable over the entire pH range to be tested. Buffers were made using established ratios of stock solutions of 0.2 M Na_2PO_4 and 0.1 M Citrate; final pH was adjusted using hydrochloric acid (HCl) or sodium hydroxide (NaOH) if needed. For SAXS and SEC, 150 mM NaCl and 2% glycerol were added. Native mass spectrometry experiments required the use of ammonium acetate buffer, and pH was adjusted using acetic acid, with the final pH value measured (see *Native Mass Spectrometry* section below). For liposome disruption assays, 10 mM Tris, 150 mM NaCl, 0.02% NaN_3, pH 8.0 was used and pH was changed by rapid acidification using 10 mM HEPES, 150 mM NaCl, 50 mM Citrate and 0.02% NaN_3 buffer at pH 3.0 as described previously(*32*), and final pH values were measured (see *Fluorescence Dequenching Liposome Leakage Assay* section below). Hexahistidine tag was removed for all experiments that tested the effect of pH.

Circular Dichroism (CD)

CD wavelength scans (260 to 195 nm) and temperature melts (25 to 95°C) were measured using a JASCO J-1500 or an AVIV model 420 CD spectrometers. Temperature melts monitored absorption signal at 222 nm and were carried out at a heating rate of 4°C/min; protein samples were at 0.25 mg/mL in either phosphate buffered saline (PBS) pH 7.4 or Na_2HPO_4-Citrate at indicated pH values (see *Buffers systems for varying pH*). Guanidinium chloride (GdmCl) titrations were all performed on an AVIV 420 spectrometer with an automated titration apparatus using either PBS pH 7.4 or Na_2HPO_4-Citrate buffers at indicated pH at room temperature, monitoring helical signal at 222 nm, using a protein concentration of 0.025 mg/mL in a 1 cm cuvette with stir bar. Each titration consisted of at least 30 evenly distributed concentration

points with one minute mixing time for each step. Titrant solution consisted of the same concentration of protein in the same buffer system plus GdmCl; GdmCl concentration of starting solutions were determined by refractive index.

Circular dichroism (CD) guanidinium chloride (GdmCl) titrations for pRO-2.3 at different pH values were measured at 25°C at 222 nm using a JASCO J-1500 spectrometer equipped with an automated titration apparatus. Titrands were Na_2HPO_4-Citrate buffer at either pH 7.00, 6.00, or 5.00, and titrants were 6M GdmCl in Na_2HPO_4-Citrate buffer at the same corresponding pH. Both titrand and titrant contained protein at a concentration of 0.025 mg/mL. Titrations ranged between 0-4M GdmCl concentration with measurements evenly distributed over 40 points in a 1 cm path length cuvette and stir bar with constant mixing at 1000 rpm.

Native Mass Spectrometry

Samples were buffer exchanged twice into 200 mM ammonium acetate (NH_4Ac; MilliporeSigma) using Micro Bio-Spin P-6 columns (Bio-Rad). Protein concentrations were determined by UV absorbance using a Nanodrop 2000c spectrophotometer (Thermo Fisher Scientific) and diluted to make up a 10-fold stock solution (50 μM and 16.7 μM monomer and trimer concentration, respectively). 1 μL of this solution was mixed with 9 μL 200 mM NH_4Ac / 50 mM triethylammonium acetate (TEAA; MilliporeSigma), adjusted with acetic acid (Fisher Scientific) to obtain the desired final pH and incubated on ice for 30 min. For experiments to test for the reversibility of disassembly, the pH was subsequently increased either by addition of ammonia or by buffer-exchange to 200 mM NH_4Ac / 50 mM TEAA (pH 7.0) via ultrafiltration (Amicon Ultra, MWCO 3 kDa). 5 μL sample were filled into an in-house pulled glass capillary

and ionized by nESI at a monomer or a trimer concentration of 5 μM or 1.67 μM, respectively. All pH titration data were acquired on an in-house modified SYNAPT G2 HDMS (Waters Corporation) with a surface-induced dissociation (SID) device incorporated between a truncated trap traveling wave ion guide and the ion mobility cell(*43*). The following instrument parameters were used: spray voltage 0.9~1.3 kV; sampling cone, 20 V; extraction cone, 2 V; source temperature, room temperature; trap gas flow, 4 mL/min; trap bias, 45V. The data were processed with MassLynx v4.1 and DriftScope v2.1. Smoothed mass spectra (mean; window 20; number of smooths 20) are shown in figs. S4 and S13. For relative quantification, charge state series were extracted from DriftScope, and smoothed spectra (mean; window 20; number of smooths 20) were integrated. Table S5 contains the observed and expected masses for all proteins in this study.

Small-angle x-ray scattering (SAXS)

Samples were purified by gel filtration in either 25 mM Tris pH 8.0 at room temperature, 150 mM NaCl, and 2% glycerol, or Na_2HPO_4-Citrate buffer at indicated pH with 150mM NaCl and 2% glycerol. For each sample, data was collected for at least two different concentrations to test for concentration-dependent effects; "high" concentration samples ranged from 4-10 mg/ml and "low" concentration samples ranged from 1-5 mg/ml (table S4). Fractions preceding the void volume of the column, or from the flow-through during concentration using spin concentrators (Millipore), were used as blanks for buffer subtraction. SAXS measurements were made at the SIBYLS 12.3.1 beamline at the Advanced Light Source. The X-ray wavelength (λ) was 1.27 Å and the sample-to-detector distance of the Mar165 detector was 1.5 m, corresponding to a scattering vector q ($q = 4\pi*\sin(\theta/\lambda)$ where 2θ is the scattering angle) range of 0.01 to 0.59 $Å^{-1}$.

Data sets were collected using 34 0.2 second exposures over a period of 7 seconds at 11 keV with protein at a concentration of 6 mg/mL. The light path is generated by a super-bend magnet to provide a 1012 photons/sec flux (1 Å wavelength) and detected on a Pilatus3 2M pixel array detector. Each sample is collected multiple times with the same exposure length, generally every 0.3 seconds for a total of 10 seconds resulting in 30-34 frames per sample. These individual spectra were averaged together over each of the Gunier, Parod, and Wide-q regions depending on signal quality over each region and frame using the FrameSlice web server (http://sibyls.als.lbl.gov/ran). The averaged spectra for each sample were analyzed using the ScÅtter software package as previously described(*29*, *44*). FoXS(*45*, *46*) was used to compare design models to experimental scattering profiles and calculate quality of fit (*X*) values.

X-ray crystallography

Purified protein samples were concentrated to 13 mg/ml for pRO-2.3 and 17 mg/ml for pRO-2.5 in 20 mM Tris pH 8.0 at room temperature with 100 mM NaCl. Samples were screened with a 5-position deck Mosquito crystallization robot (ttplabtech) with an active humidity chamber, utilizing JCSG Core I-IV screens (Qiagen). Crystals were obtained after 2 to 14 days by the sitting drop vapor diffusion method with the drops consisting of a 1:1, 2:1 and 1:2 mixture of protein solution and reservoir solution. The conditions that resulted in the crystals used for structure determination are as follows: pRO-2.3 crystallized in JCSG-I B7, which consists of 0.2M di-sodium tartrate and 20% w/v PEG 3350; pRO-2.5 crystalized in JCSG-I A9, which consists of 0.2 M Potassium acetate and 20% w/v PEG 3350.

X-ray data collection and structure determination

Protein crystals were looped and placed in reservoir solution containing 20% (v/v) glycerol as a cryoprotectant, and flash-frozen in liquid nitrogen. Datasets were collected at the Advanced Light Source at Lawrence Berkeley National Laboratory with beamlines 8.2.1 and 8.2.2. Data sets were indexed and scaled using XDS(*47*). Phase information was obtained by molecular replacement using the program PHASER(*48*) from the Phenix software suite(*49*); computational design models were used for the initial search. Following molecular replacement, the models were improved using Phenix.autobuild(*50*); efforts were made to reduce model bias by setting rebuild-in-place to false, and using simulated annealing and prime-and-switch phasing. Iterative rounds of manual building in COOT(*51*) and refinement in Phenix were used to produce the final models. Due to the high degree of self-similarity inherit in coiled-coil-like proteins, datasets for the reported structures suffered from a high degree of pseudo translational non-crystallographic symmetry, as report by Phenix.Xtriage, which complicated structure refinement and may explain the higher than expected R-values reported. RMSDs of bond lengths, angles and dihedrals from ideal geometries were calculated using Phenix(*49*). The overall quality of the final models was assessed using MOLPROBITY(*52*). Supplementary able S2 summarizes diffraction data and refinement statistics.

Liposome Preparation and Characterization

Liposomes composed of DOPC (1,2-dioleoyl-sn-glycero-3-phosphocholine), DOPC with 25% cholesterol (molar ratio to DOPC), 3:1 DOPC:POPS (1-palmitoyl-2-oleoyl-sn-glycero-3-phospho-L-serine), and 3:1 DOPC:POPS with 25% cholesterol were prepared identically to a final concentration of 5 mM total lipid as previously described(*32*); lipids from Avanti Polar Lipids. Lipids solubilized in chloroform were dried under nitrogen gas and stored under vacuum

for a minimum of 2 hours to remove residual solvent. The dried lipid film was the resuspended in Tris buffer (10 mM Tris, 150 mM NaCl, and 0.02% NaN_3 pH 8.0) containing 25 mM Sulforhodamine B (SRB) fluorophore (Sigma) and subjected to 10 sequential freeze thaw cycles in liquid nitrogen. Liposomes were extruded 29 times through 100 nm pore size polycarbonate filters (Avanti Polar Lipids) and purified from free fluorophore using a PD-10 gel filtration column (GE Healthcare) into storage buffer (10 mM Tris, 150 mM NaCl, and 0.02% NaN_3 pH 8.0). Liposome size and homogeneity was analyzed by dynamic light scattering (DLS) using a Dynapro Nanostar DLS (Wyatt Technologies). On average liposome diameter ranged from 120-130 nm with low polydispersity. Liposomes were stored at 4°C and used within 5 days of preparation.

Fluorescence Dequenching Liposome Leakage Assay

Liposome disruption and content leakage was analyzed by fluorescence spectroscopy as previously described(*32*). Liposomes containing SRB fluorophore at self-quenching concentrations were incubated with 2.5 μM peptide, with respect to monomer, at 24°C and pH 8.0 in Tris buffer (10 mM Tris, 150 mM NaCl, 0.02% NaN_3, pH 8.0) for 10 minutes. The solution was rapidly acidified to the target pH by addition of a fixed volume of acidification buffer and incubated for 20 minutes. Acidification buffers are mixtures of the Tris pH 8.0 buffer and citrate buffer pH 3.0 (10 mM HEPES, 150 mM NaCl, 50 mM citrate and 0.02% NaN_3 pH 3.0) in empirically determined ratios to achieve the target pH. SRB fluorescence is independent of pH within the ranges used here(*32*). Finally, Triton X-100 (Sigma) was added to a final concentration of 1% to fully disrupt liposomes. Liposome disruption as indicated by content leakage and SRB dequenching was normalized using the formula $[F_{(t)}-F_{(0)}]/[F_{(Max)}-F_{(0)}]$ where $F_{(0)}$

is the average fluorescence intensity before acidification and $F_{(Max)}$ is the average fluorescence intensity after addition of Triton X-100. All measurements were collected on a Varian Cary Eclipse spectrophotometer using an excitation/emission pairing of l 565/586 and 2.5 nm slit widths at 24°C. Any data plotted together was collected using the same batch of liposomes.

Cryo-EM Specimen Preparation and Imaging

Designs pRO-2, pRO-2 I56V, and pRO-2-noHis were chemically conjugated to 10 nm Gold nanoparticles according to manufacturer's instructions, ensuring all gold nanoparticles were conjugated to protein (abcam). The conjugation reactions were performed immediately prior to use for electron microscopy imaging. For each design pRO-2, pRO-2 I56V, and pRO-2-noHis a solution of 2.5 μM purified protein, 0.125 μM gold-conjugated protein, and 1 mM DOPC liposomes was applied to glow-discharged C-Flat 2/2-2C-T holey carbon grids (Protochips, Inc.) and acidified on the grid by addition of HEPES-citrate buffer. The grids were prepared using a Vitrobot Mark IV (FEI) at 4C and 100% humidity before being plunge-frozen in ethane cooled with liquid nitrogen.

Electron micrographs were collected using a Tecnai G2 Spirit Transmission Electron Microscope (FEI) operated at 120kV and equipped with a 4k x 4k Gatan Ultrascan CCD camera at a nominal magnification of 26,000x or a Tecnai TF-20 Transmission Electron Microscope (FEI) operated at 200kV equipped with a K2 Summit Direct Electron Detector (Gatan).

Projection micrographs collected on the TF-20 were captured with the detector operating in counting mode. Specimens were imaged at 14,500 magnification, giving a pixel size of 0.254nm, with a dose of ~18e-/ $Å^2$ across 75 200ms movie frames. Data were collected in a semi-automated fashion using Leginon(*53*) and micrograph movie frames were aligned using MotionCor2(*54*).

Leginon was used to collect tomography tilt series from -48 to +48 degrees bidirectionally in 3 degree increments with a total accumulated dose of ~100 e-/Å^2. Reconstructions were processed using etomo in the IMOD software suite(*55*) with CTF parameters estimated from CTFFIND4(*56*). Reconstructed tomograms were visualized and measurements were made using ImageJ(*57*).

Cell Culture, Plating, and Transfection

U-2 OS (ATCC) cells were cultured in DMEM supplemented with 10% (v/v) inactivated FBS (Corning), 2 mM glutamine, penicillin (100 IU/mL), and streptomycin (100 µg/mL) at 37 ºC and 5% CO2. The glass-bottom coverslip chambers were pre-coated with 500 µg/mL of Matrigel (Corning). Transfection of LAMP1-HaloTag was performed using Lonza Nucleofector system according to the manufacturer's specifications. After overnight of recovery and expression, the cells expressing LAMP1-HaloTag were labeled with 100 nM JF646-HTL for 30 minutes and washed three times with pre-warmed DMEM medium.

Live Cell Experiments

The final concentration of 5 µM +36GFP fusion proteins was incubated with the LAMP1-HaloTag expressing U-2 OS cells on a pre-coated coverslip for 1 hr. Cells were fixed with 4% paraformaldehyde for 20 min at room temperature (RT) and quenched/rinsed with PBS supplemented with 30 mM glycine. Then, the coverslips were mounted on FluoroSave (Millipore). For pH measurement of the lysosome, LysoSensor Yellow/Blue DND-160 was incubated at 1 mg/mL overnight and washed twice prior to imaging(*58*). The final concentration of 5 µM protein was incubated with the LAMP1-HaloTag expressing U2-OS cells that were loaded with 1 mg/mL LysoSensor Yellow/Blue DND-160 for 1 hr. In separate chambers,

LysoSensor Yellow/Blue DND-160 loaded cells were incubated with bafilomycin A1 (1 μM) and chloroquine (50 μM) for 1 hr as a control.

Confocal Microscopy

For fixed cell confocal microscopy, a customized Nikon TiE inverted scope outfitted with a Yokogawa spinning-disk scan head (#CSU-X1) along with an Andor iXon EM-CCD camera (DU-897) with 100-ms exposure time was used to collect 3D images using an SR Apo TIRF 100X 1.49 oil-immersion objective. Mender's coefficients were calculated in 3D with JF646 signal (LAMP1-HaloTag) and +36GFP signal (corresponding proteins) using Imaris software with thresholding. Zeiss 880 equipped with AiryScan was also used to obtain high resolution images using a Plan-Apocrhomatic 63x/1.4 oil DIC objective.

For live cell confocal microscopy, Zeiss 880 was used to collect LysoSensor Yellow/Blue signal. LysoSensor Yellow/Blue was excited with a 405 nm laser, and its emission was collected into the two regions (Blue = 410-499 nm Yellow = 500-600 nm) using a Plan-Apochromat 63x/1.4 oil DIC objective. The ratio of the two channels was calculated using the home-built software in Matlab.

Visualization and figures

All structural images for figures were generated using PyMOL(*59*)**.**

Theoretical modeling and fitting to native mass spectrometry data

Python scripts were written to generate theoretical curves according to Equations S1-S2, and curve-fitting to native mass spectrometry data (Figures 1, 3, 5) according to Equation S3,

implemented by nonlinear least squares using curve_fit from scipy.optimize(*60*). The free energy estimates for individual *n*, *m*, and *l* layers used in Equation S2 modeling were estimated by solving linear equations as follows: values for the free energy of unfolding for designs pRO-2 and variants were estimated from GdmCl denaturation experiments (fig. S6); each of these designs have different numbers of *n*, *m*, and *l* layers, thus series of linear equations relating the number of each layer type to the total free energies of unfolding were solved to estimate dG values of the individual layers of each type. These free energy estimates for the individual *n*, *m*, and *l* layers were then used in the theoretical modeling (Eq. S2) shown in Figure 3C. All scripts and data are available in the following github repository:

https://github.com/sboyken/pHresponsiveOligomers

Supplementary Figures S1-S15

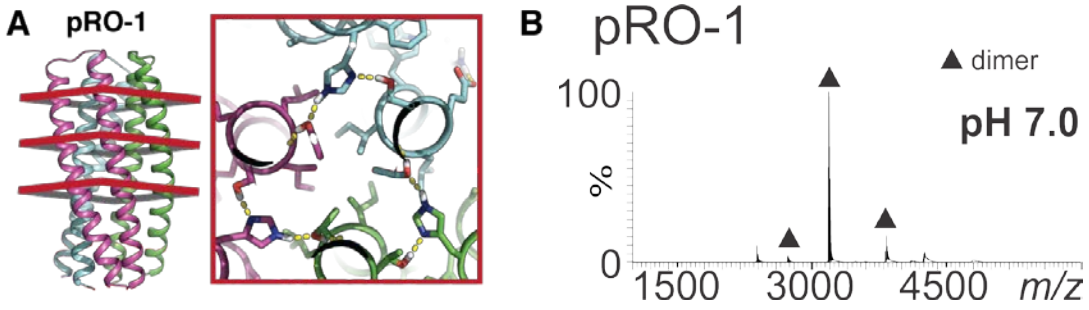

Fig. S1. (**A**) Homotrimer design pRO-1 was shown to be primarily dimeric at 7.5 μM dimer concentration by (**B**) native mass spectrometry. The mass spectrum was acquired on an Exactive Plus EMR Orbitrap mass spectrometer (Thermo Scientific) modified with a quadrupole mass filter and an SID device(*56*). Unlike successful designs pRO-2 to 5, which have contiguous, extensive histidine networks at each cross section, pRO-1 consists of three separate disjoint networks at each cross section, each with only a single histidine.

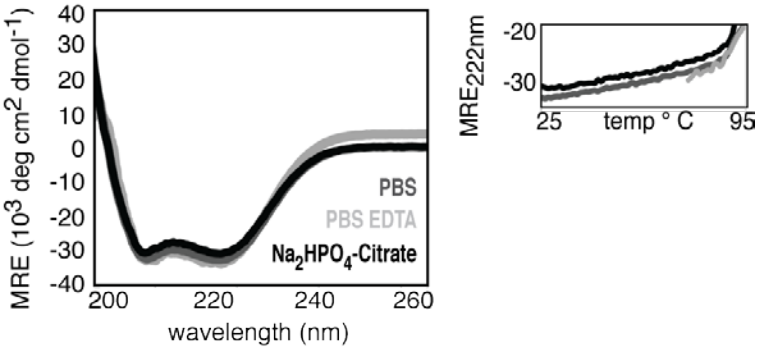

Fig. S2. EDTA and Na_2HPO_4-Citrate buffer system do not affect the fold or thermostability. Design pRO-2 CD wavelength scan and temperature melt monitoring 222 nm (*inset*) for pRO-2 in Na_2HPO_4-Citrate buffer pH 7.0 (black), PBS pH 7.4 (dark gray), and PBS pH 7.4 with 10mM EDTA (light gray).

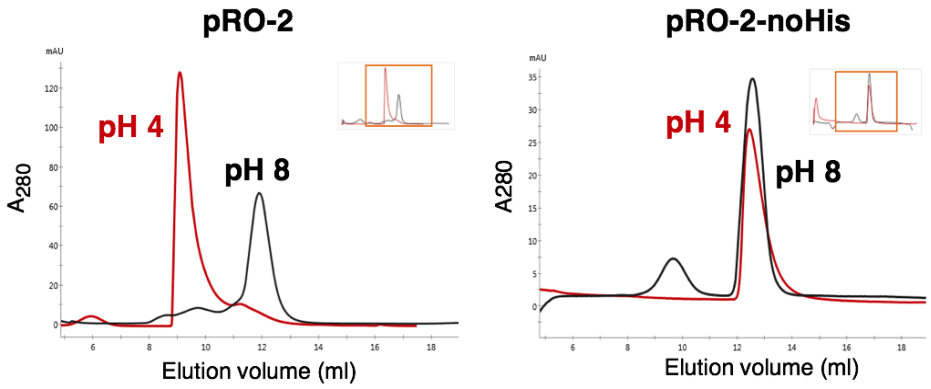

Fig. S3. Design pRO-2 is pH-responsive by size-exclusion chromatography (SEC), whereas design pRO-2-noHis is not: SEC chromatograms using a Superdex^{TM} 75 column and 25mM Tris pH 8.0 at room temperature (black) or Na_2HPO_4-Citrate buffer at pH 4 (red). Design pRO-2 is a soluble aggregate at pH 4 under these conditions, whereas by native mass spectrometry, pRO-2 is predominantly monomeric at pH 4 (Figure 1C); differences could be explained by different buffer systems or the vacuum conditions of the native mass spectrometry.

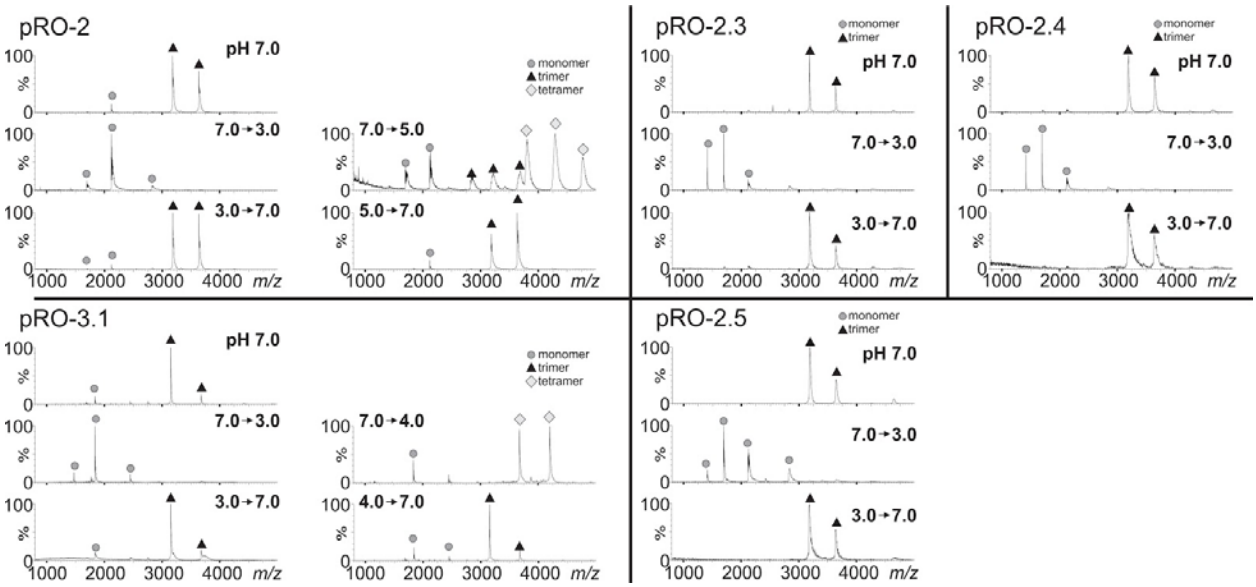

Fig. S4. Reversibility of disassembly as determined by native mass spectrometry. 5 μM pRO-2 and pRO-3.1 trimer and 6.67 μM pRO-2.3, pRO-2.4 and pRO-2.5 trimer were measured in 200 mM NH_4Ac / 50 mM TEAA (pH 7.0). Acetic acid was added to decrease the pH from 7.0 → 3.0, which caused dissociation of trimers into monomers. Returning to neutral pH (3.0 → 7.0) results in re-association of monomers into trimer. In the case of pRO-2.3, pRO-2.4 and pRO-2.5, re-association was induced via buffer-exchange to 200 mM NH_4Ac / 50 mM TEAA (pH 7.0) by ultrafiltration (Amicon Ultra, MWCO 3 kDa). In case of pRO-2 and pRO-3.1, pH neutralization was accomplished by multiple rounds exchange to 200 mM NH_4Ac / 50 mM TEAA (pH 7.0) by microdialysis (Pierce 96-well microdialysis plates. MWCO 3.5 kDa). Designs pRO-2 and pRO-3.1 exhibit the formation of a tetramer intermediate at pH ~5.0

and ~4.0, respectively; returning to neutral pH (5.0 → 7.0 for pRO-2, or pH 4.0 → 7.0 for pRO-3.1) shows that these tetramer intermediates are also reversible back to trimer.

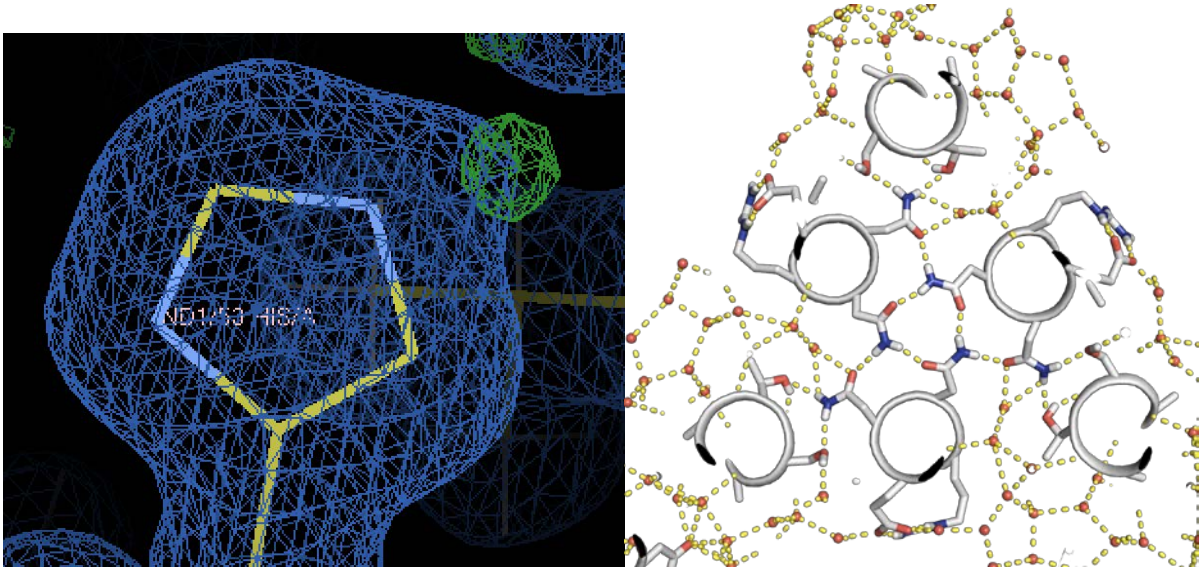

Fig. S5. 1.28 Å X-ray crystal structure of design pRO-2 (PDB ID 6MSQ): (*left*) during refinement, positive (green) density was observed from the difference map where the proton is supposed to be in the designed hydrogen bond network. (*right*) The non-histidine polar network, layer *l*, extends to make additional hydrogen bonds with resolved water molecules as part of a very extensive hydrogen bond network.

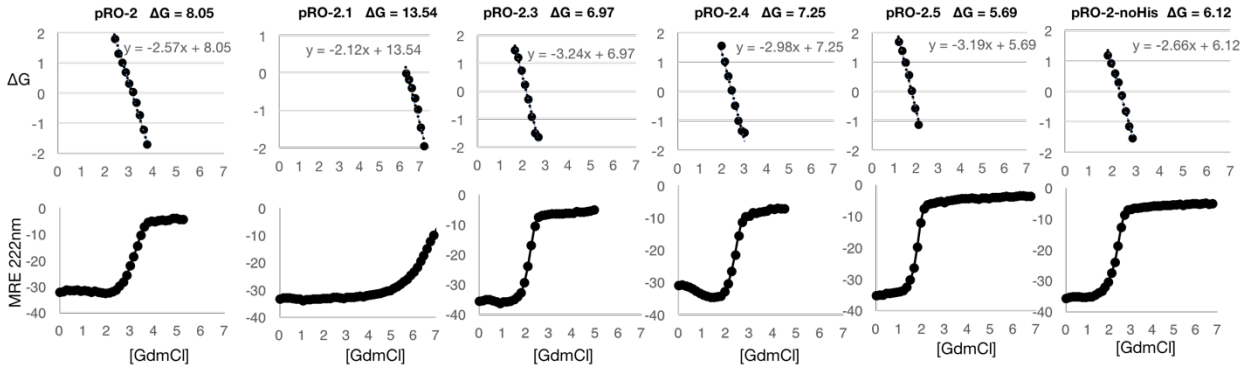

Fig. S6. ΔG estimates in kcal/mol (*top*) from GdmCl denaturation experiments (*bottom*); from this data, ΔG for each individual layer type (*n, m, l*) were estimated by solving a set of linear equations given the ΔG of unfolding for each design and its corresponding number of layers of each type (see Supplemental section *Modeling free energy of assembly of trimer designs with variable numbers of hydrophobic, polar, and histidine containing layers*); these values were then used for the model (Eq. S2) to generate the theoretical dissociation curves in Figures 3C and 5A.

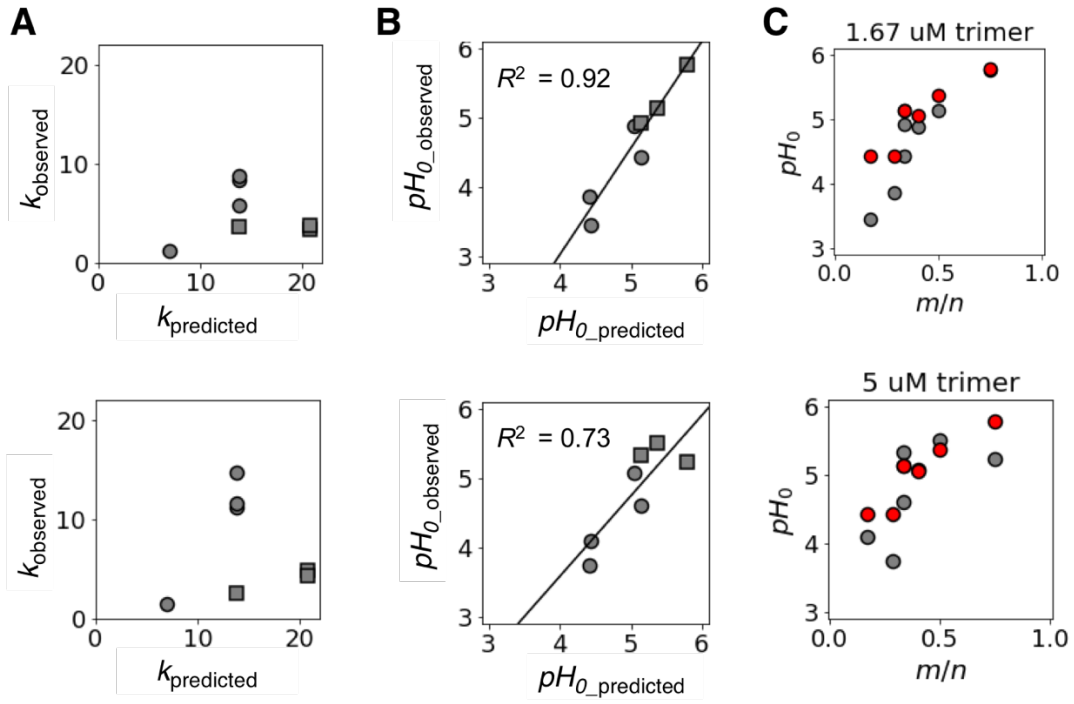

Fig. S7. Predicted vs experimentally observed values for (**A**) cooperativity (*k*) and (**B**) transition pH (pH_0); squares denote designs with histidine networks close to their termini; R^2 values were determined by simple linear regression. **(C)** Observed (gray) and predicted (red) transition pH_0 versus the ratio of *m* (histidine network layers) to *n* (hydrophobic layers). Values for $k_{observed}$ and $pH_{0\_observed}$ were obtained from fitting native mass spectrometry data (Figure 3D) to Equation S3: data was collected at a protein concentration of (*top row*) 1.67 μM or (*bottom row*) 5 μM with respect to the trimeric species. Predicted values for pH_0 were obtained from Equation S4, which relates Equations S2 and S3 to predict pH_0 as a function of *n*, *m*, and *l*; and $k_{predicted}$ can be approximated by $3m \cdot \ln(10)$.

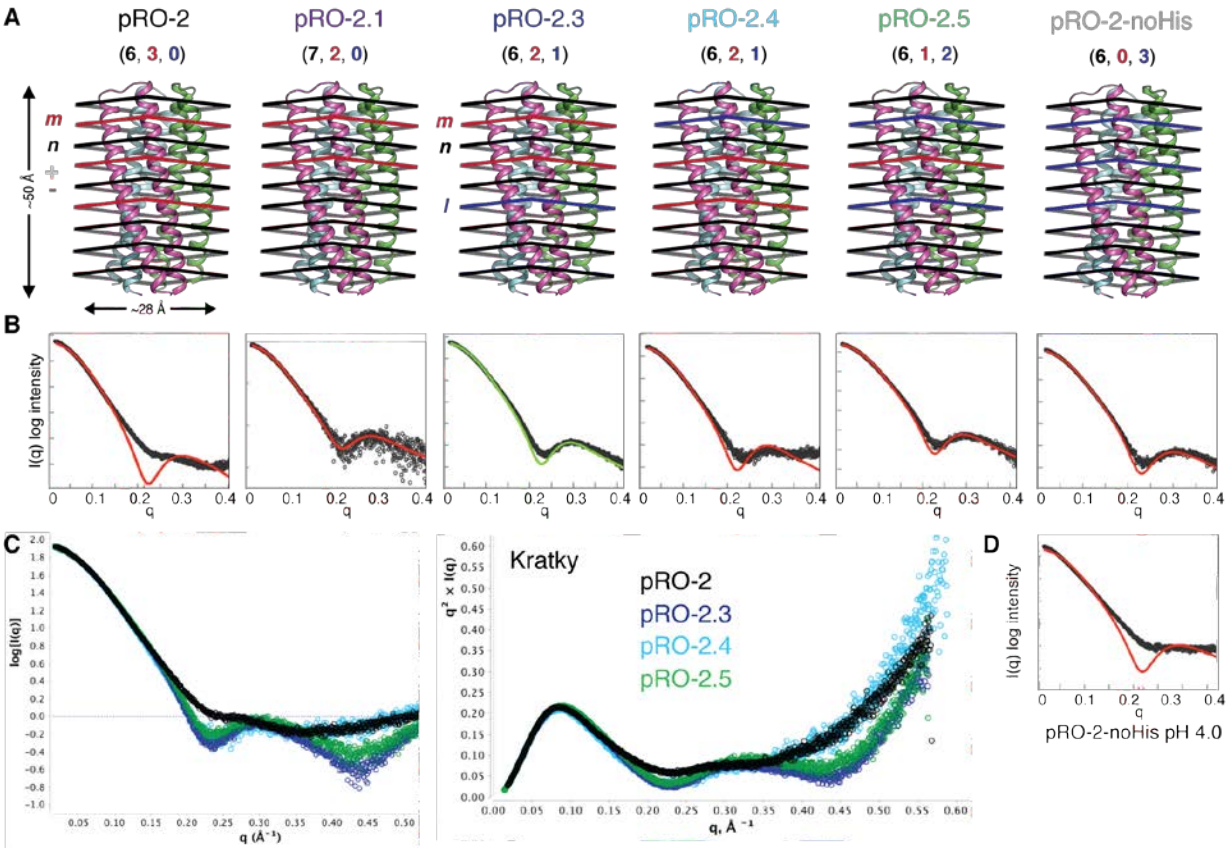

Fig. S8. Small-angle X-ray scattering (SAXS) to assess flexibility. SAXS profiles of (**A**) designs pRO-2, pRO-2.1, pRO-2.3. pRO-2.4, pRO-2.5, and pRO-2-noHis: (**B**) experimental scattering data (black) at pH 8.0 is in close agreement with theoretical profiles computed from design models (red) using FoXS(*41*, *42*). However, there are differences noticeable differences between designs that have a histidine network close to the termini (pRO-2 and pRO-2.4) compared to those that do not (pRO-2.1, pRO-2.3, pRO-2.5, and pRO-2-noHis): (**C**) Scaled Log10 intensity plots (*left*) and Kratky plots (*right*) show that pRO-2 (black) and pRO-2.4 (cyan) are similar, with spectra consistent with increased flexibility as compared to pRO-2.3 and pRO-2.5. (**D**) pRO-2-noHis at pH 4.0 shows subtle differences in the high q region, but is still in close agreement in the low q, Gunier region, and consistent with a trimeric species. Plots in (C) made using ScÅtter software package (*29*, *40*).

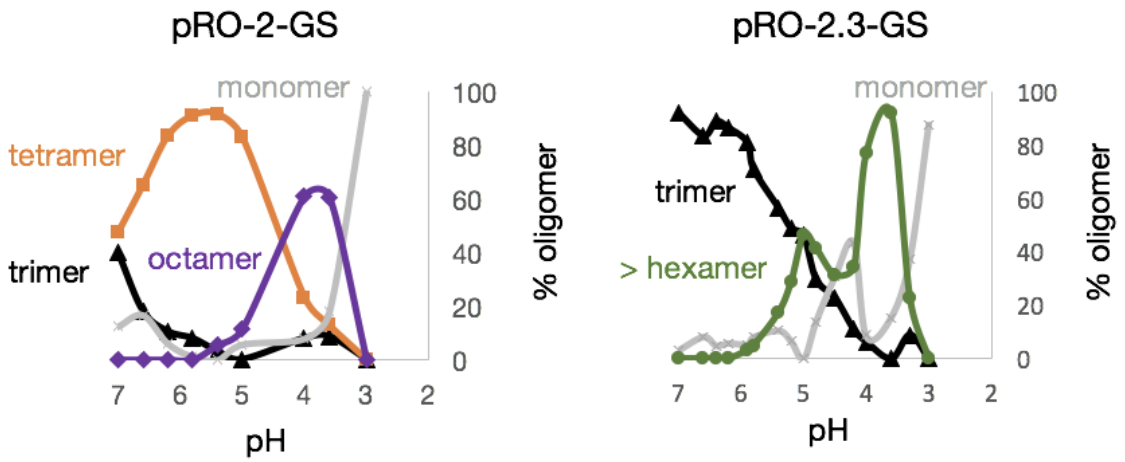

Fig. S9. Other factors that affect cooperativity; the role of the helical hairpin loop. Replacing the structured hairpin loop connecting the helices of the monomer with a flexible GS linker results in less cooperativity, as assessed by native mass spectrometry at different pH values. (*left*) Design pRO-2-GS loses its homogenous trimeric assembly at neutral pH when the flexible loop is introduced. (*right*) Design pRO-2.3.-GS retains its trimeric assembly at neutral pH, but disassembles with less cooperativity (steepness of transition) in response to lower pH than its parent design (Figure 3D).

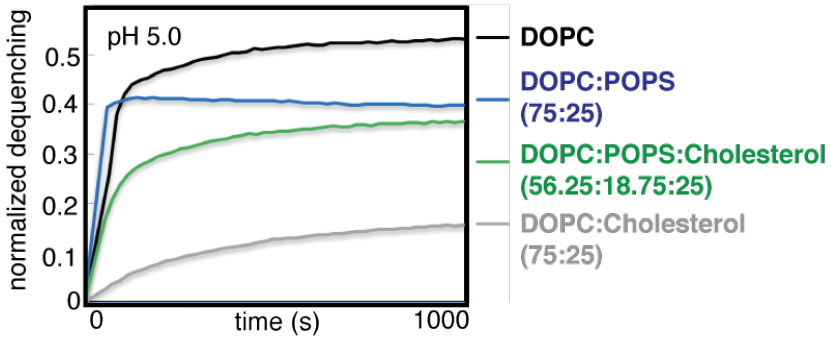

Fig. S10. Liposome disruption assay (as in Figure 4) for design pRO-2 at pH 5.0 using liposomes with more native-like lipid compositions.

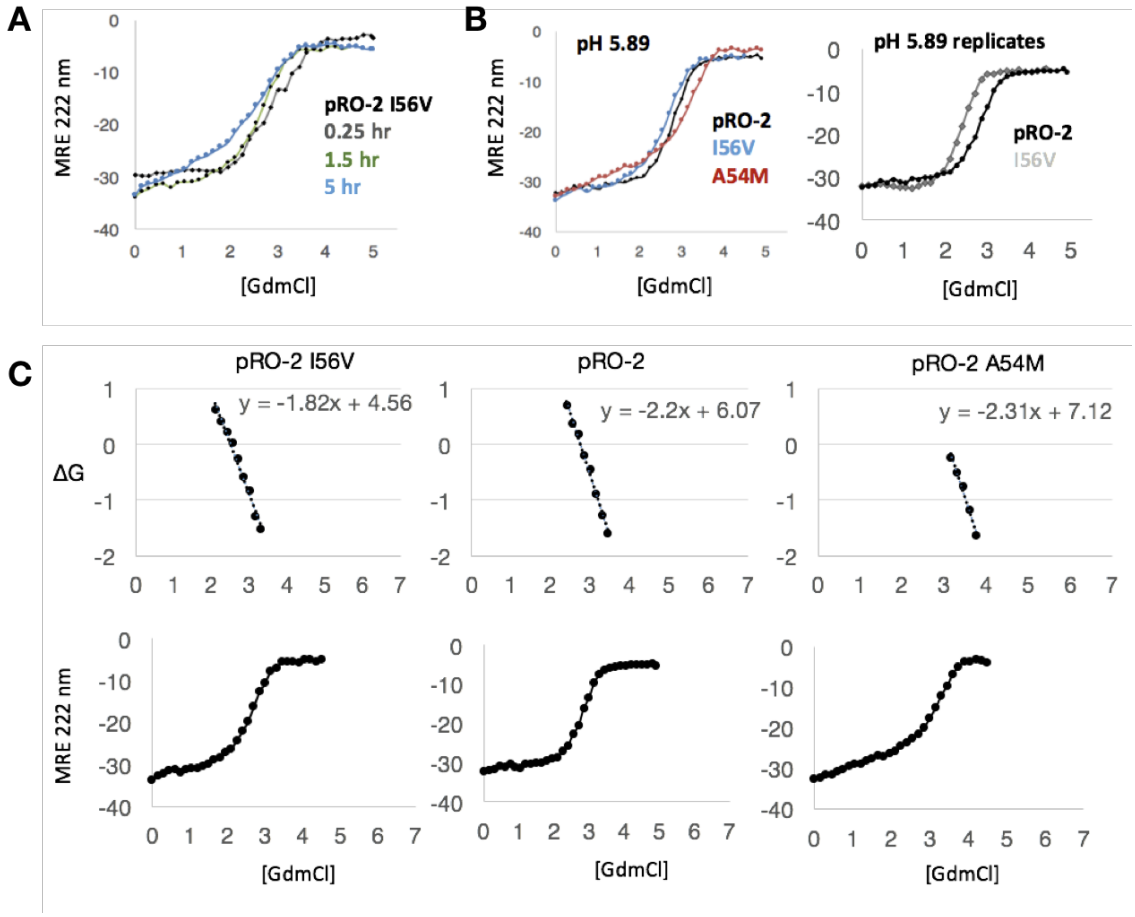

Fig. S11. CD data for pRO-2 mutants I56V and A54M. (A-B) GdmCl denaturation experiments performed at pH 5.89 in Na_2HPO_4-Citrate buffer. (A) Letting the samples sit at low pH for different amounts of time before starting experiments affected results; for this reason, all native MS and CD data at varying pH's in this study were incubated for the same short amount of time before starting each experiment to ensure consistency. (B) I56V and A54M show subtle, but reproducible, changes in stability (data shown is representative from three independent experiments). (C) Free energy of unfolding calculations from denaturation experiments as in Fig. S6.

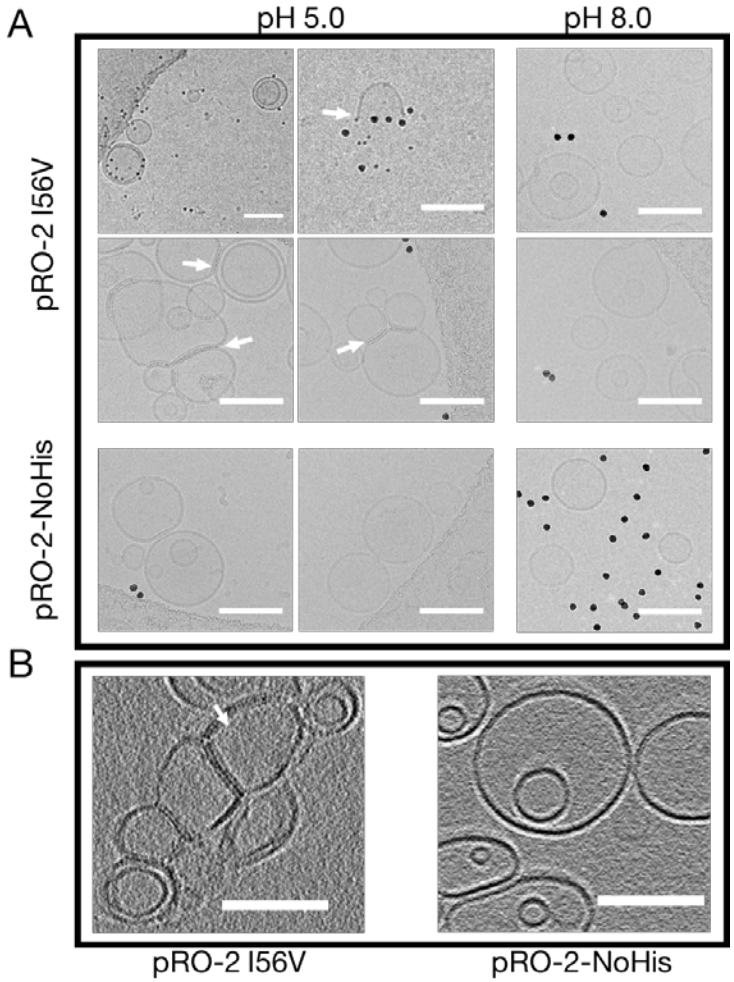

FIg. S12. (**A**) **Representative electron micrographs of DOPC liposomes and purified designed proteins pRO-2 I56V and pRO-2-NoHis conjugated to 10nm gold nanoparticles at pH 5**. Free and gold conjugated pRO-2 I56V are membrane active and associate with liposomes at pH 5. Two primary modes of interaction are observed (Indicated by white arrows): liposome disruption, where the lipid bilayer appears ruptured and discontinuous, and bilayer bridging, where a tight and extended interface is formed between two liposomes. Density that likely corresponds to pRO-2 I56V can be seen at the interface. Design pRO-2 I56V does not perturb liposomes at pH 8 and the protein conjugated gold nanoparticles are well dispersed and not associated with liposomes. Design pRO-2-NoHis was similarly membrane inactive at pH 5 and 8. (**B) Reconstructed cryo-electron tomograms of DOPC liposomes with designs pRO-2 I56V (left) or pRO-2-NoHis (right) at pH 5**. At pH 5, pRO-2 I56V helps create extended interfaces between adjacent liposomes. Design pRO-2-NoHis does not exhibit any membrane activity at pH 5. All scale bars are 100nm.

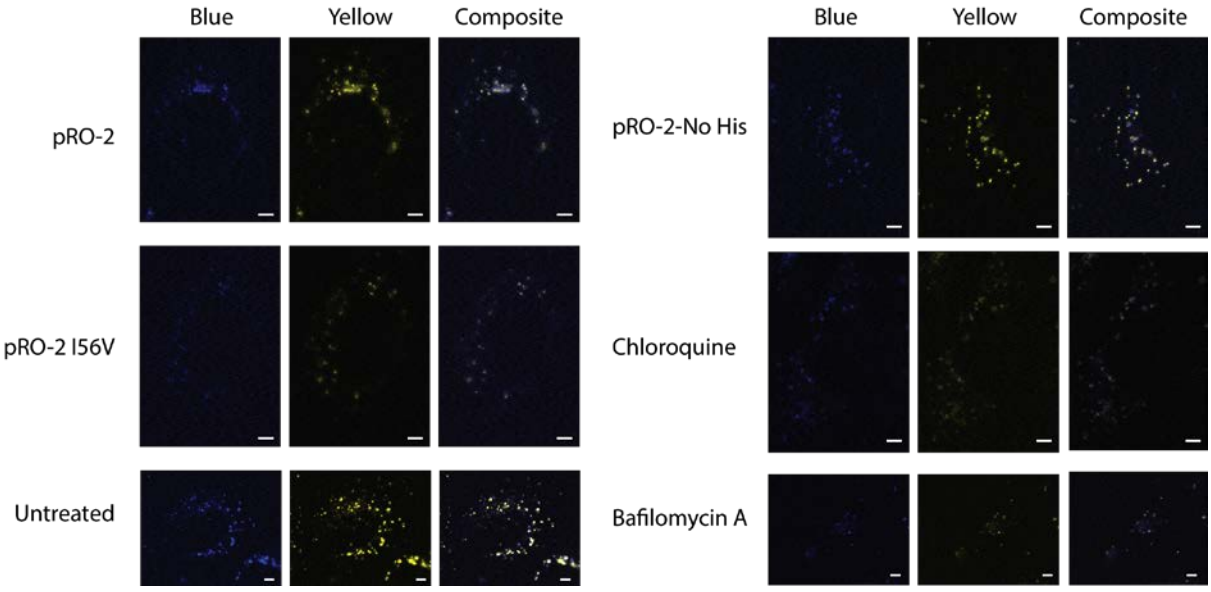

Fig. S13. Images of U2-OS cells loaded with LysoSensor Yellow/Blue DND-160 that are incubated with pRO-2 (5 μM, top left), pRO-2 I56V (5 μM, middle left), Untreated (bottom left), pRO-2-No His (5 μM, top right), Chloroquine (50 μM, middle right), Bafilomycin A (1 μM, bottom right) for 1 hr. Blue images represent intensities of emission acquired in the region of 410-499 nm upon 405 nm excitation. Yellow images represent intensities of emission acquired in the region of 500-600 nm upon 405 nm excitation. Intensity of excitation laser was same for all images and images are scaled to the same maximum intensity value.

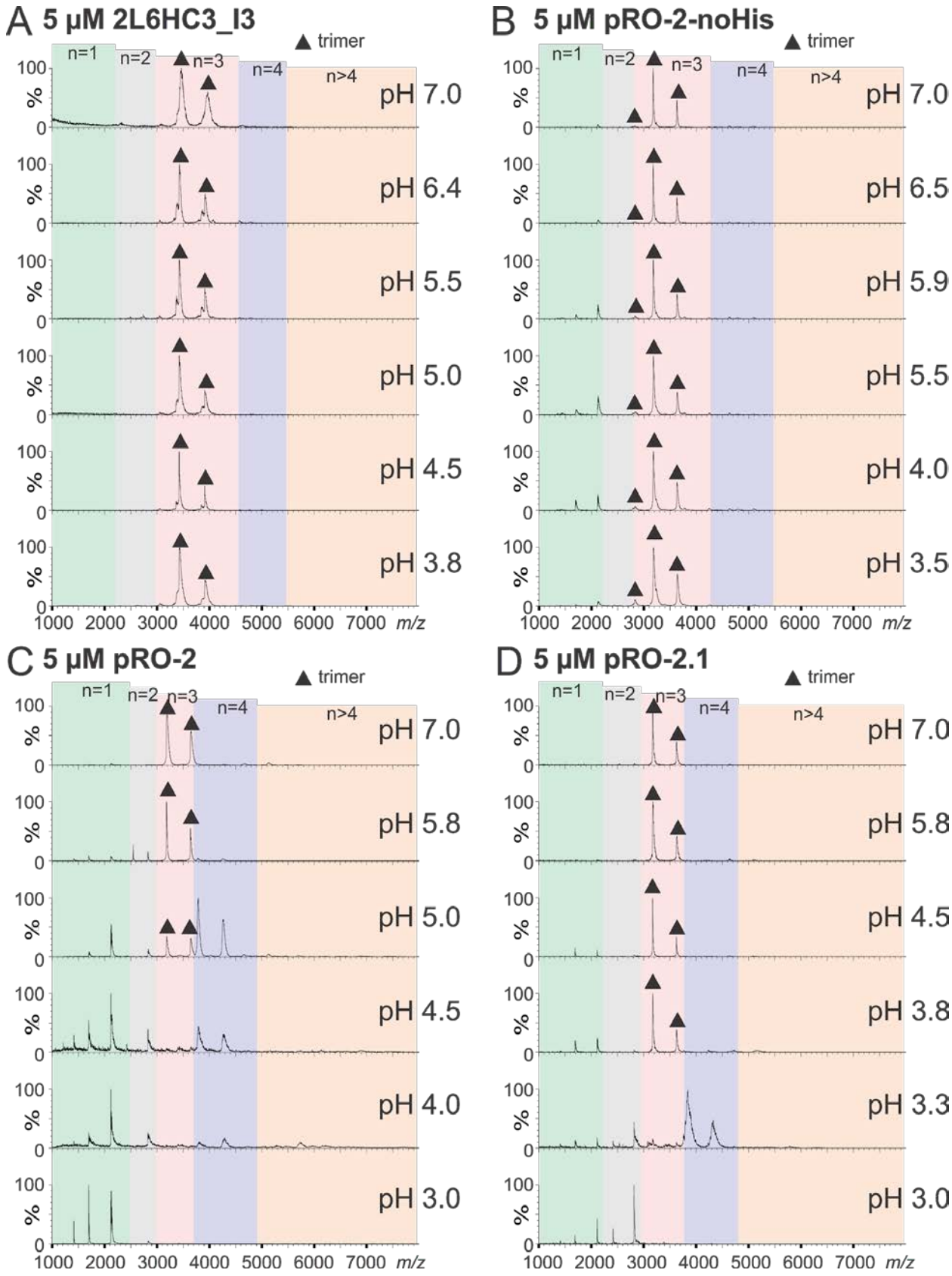
A 5 µM 2L6HC3_I3
B 5 µM pRO-2-noHis
C 5 µM pRO-2
D 5 µM pRO-2.1
trimer
n=1
n=2
n=3
n=4
n>4
pH 7.0
pH 6.4
pH 5.5
pH 5.0
pH 4.5
pH 3.8
pH 6.5
pH 5.9
pH 4.0
pH 3.5
pH 5.8
pH 3.3
pH 3.0
100
%
0
1000 2000 3000 4000 5000 6000 7000 m/z

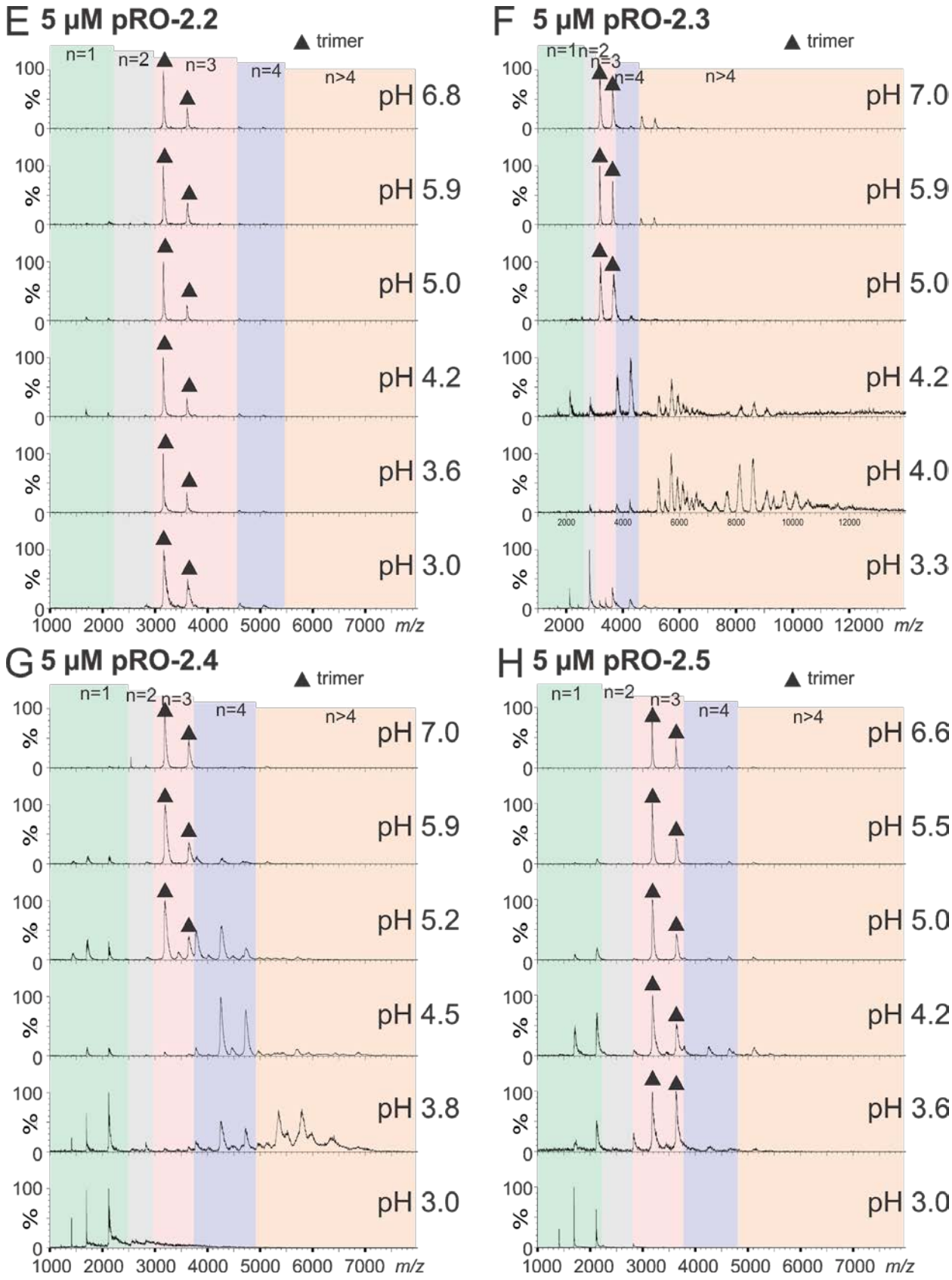
E 5 µM pRO-2.2
F 5 µM pRO-2.3
G 5 µM pRO-2.4
H 5 µM pRO-2.5
trimer
n=1
n=2
n=3
n=4
n>4
pH 6.8
pH 5.9
pH 5.0
pH 4.2
pH 3.6
pH 3.0
pH 7.0
pH 4.0
pH 3.3
pH 5.2
pH 4.5
pH 3.8
pH 6.6
pH 5.5
100
%
0
1000 2000 3000 4000 5000 6000 7000 m/z
2000 4000 6000 8000 10000 12000 m/z

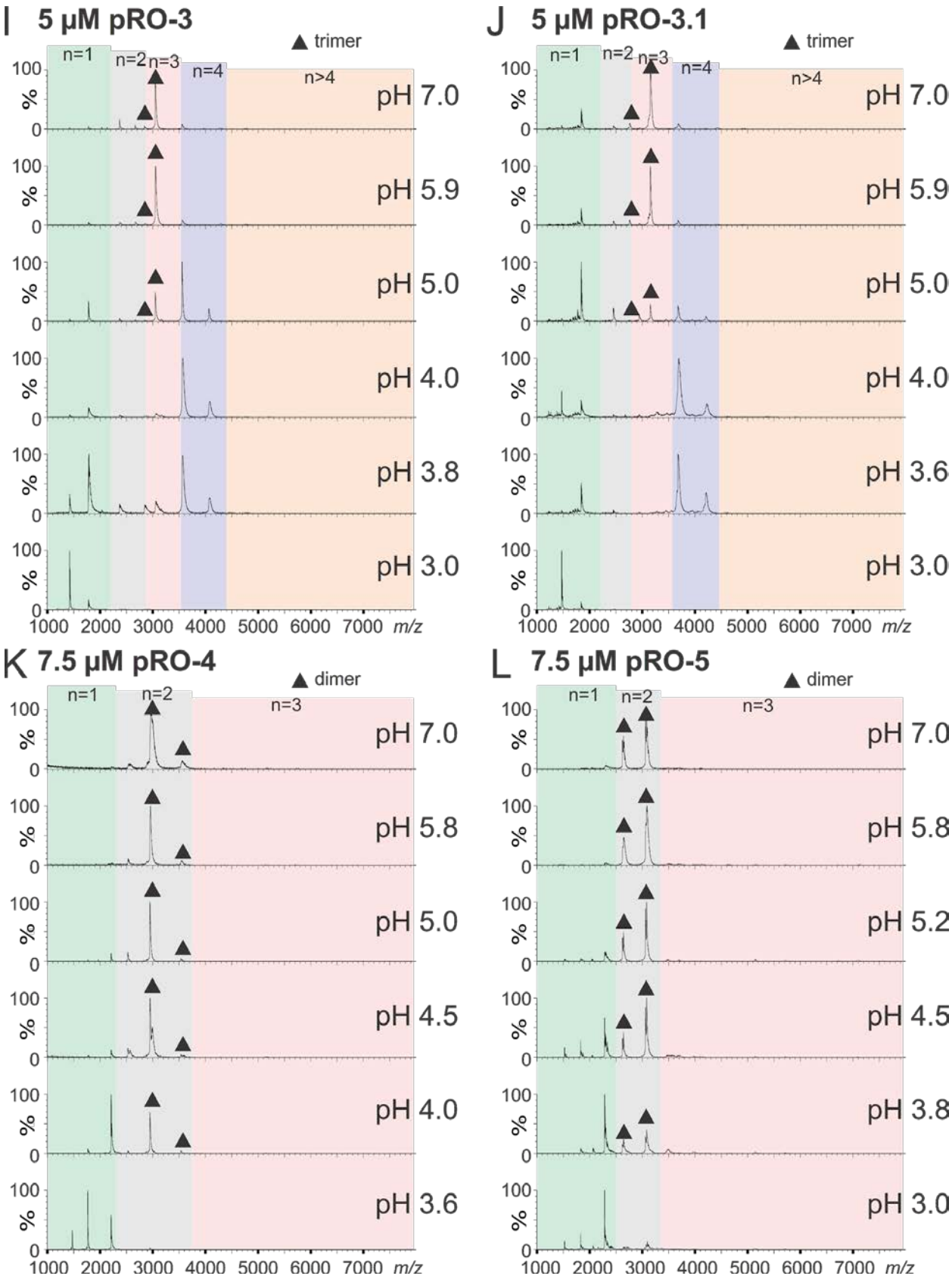
I 5 µM pRO-3
trimer
n=1
n=2
n=3
n=4
n>4
pH 7.0
pH 5.9
pH 5.0
pH 4.0
pH 3.8
pH 3.0
100
%
0
1000 2000 3000 4000 5000 6000 7000 m/z
J 5 µM pRO-3.1
trimer
pH 7.0
pH 5.9
pH 5.0
pH 4.0
pH 3.6
pH 3.0
K 7.5 µM pRO-4
dimer
n=1
n=2
n=3
pH 7.0
pH 5.8
pH 5.0
pH 4.5
pH 4.0
pH 3.6
L 7.5 µM pRO-5
dimer
pH 7.0
pH 5.8
pH 5.2
pH 4.5
pH 3.8
pH 3.0

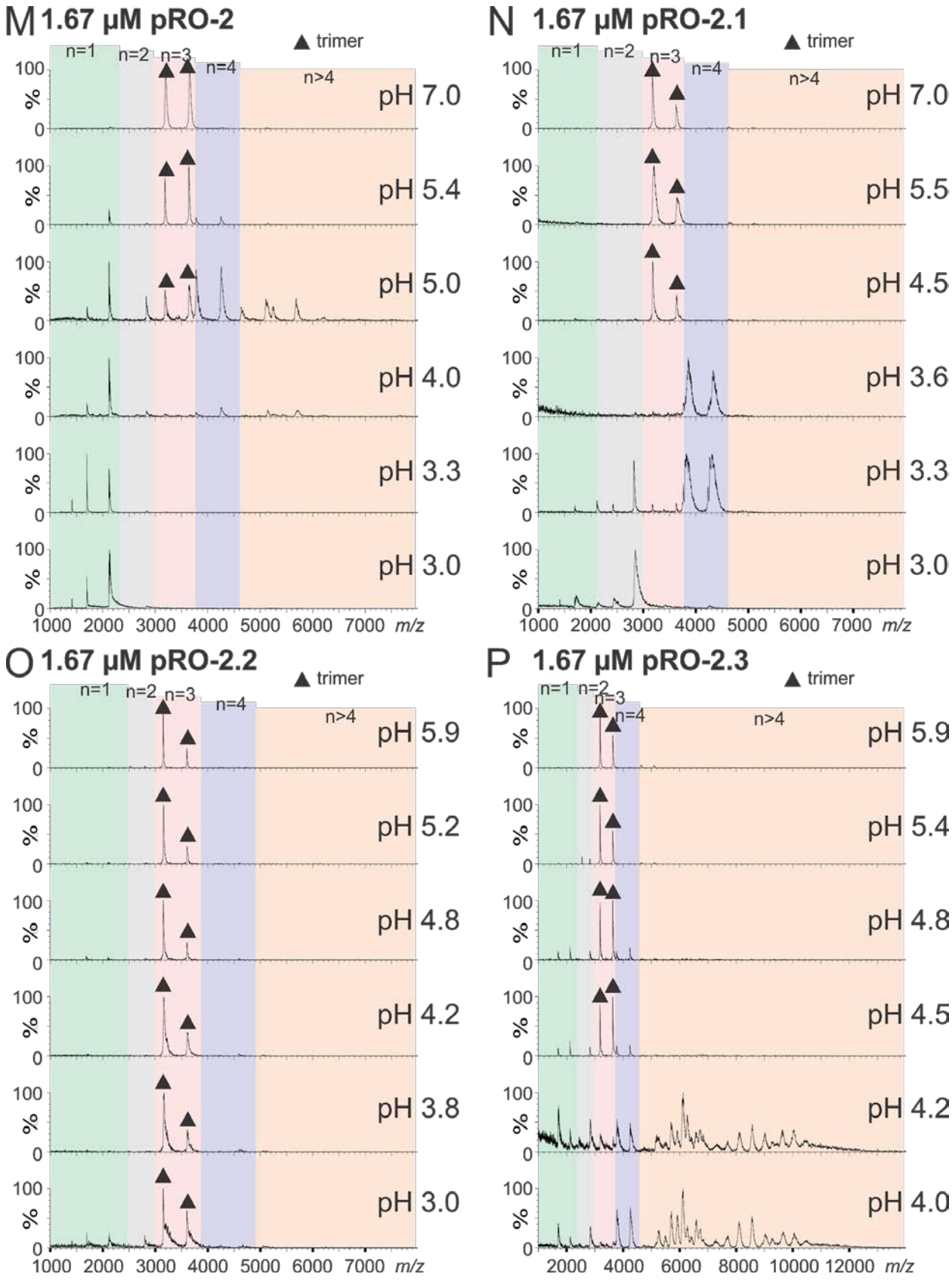
M 1.67 µM pRO-2
N 1.67 µM pRO-2.1
O 1.67 µM pRO-2.2
P 1.67 µM pRO-2.3
trimer
n=1
n=2
n=3
n=4
n>4
pH 7.0
pH 5.4
pH 5.0
pH 4.0
pH 3.3
pH 3.0
pH 5.5
pH 4.5
pH 3.6
pH 5.9
pH 5.2
pH 4.8
pH 4.2
pH 3.8
pH 4.0
%
m/z

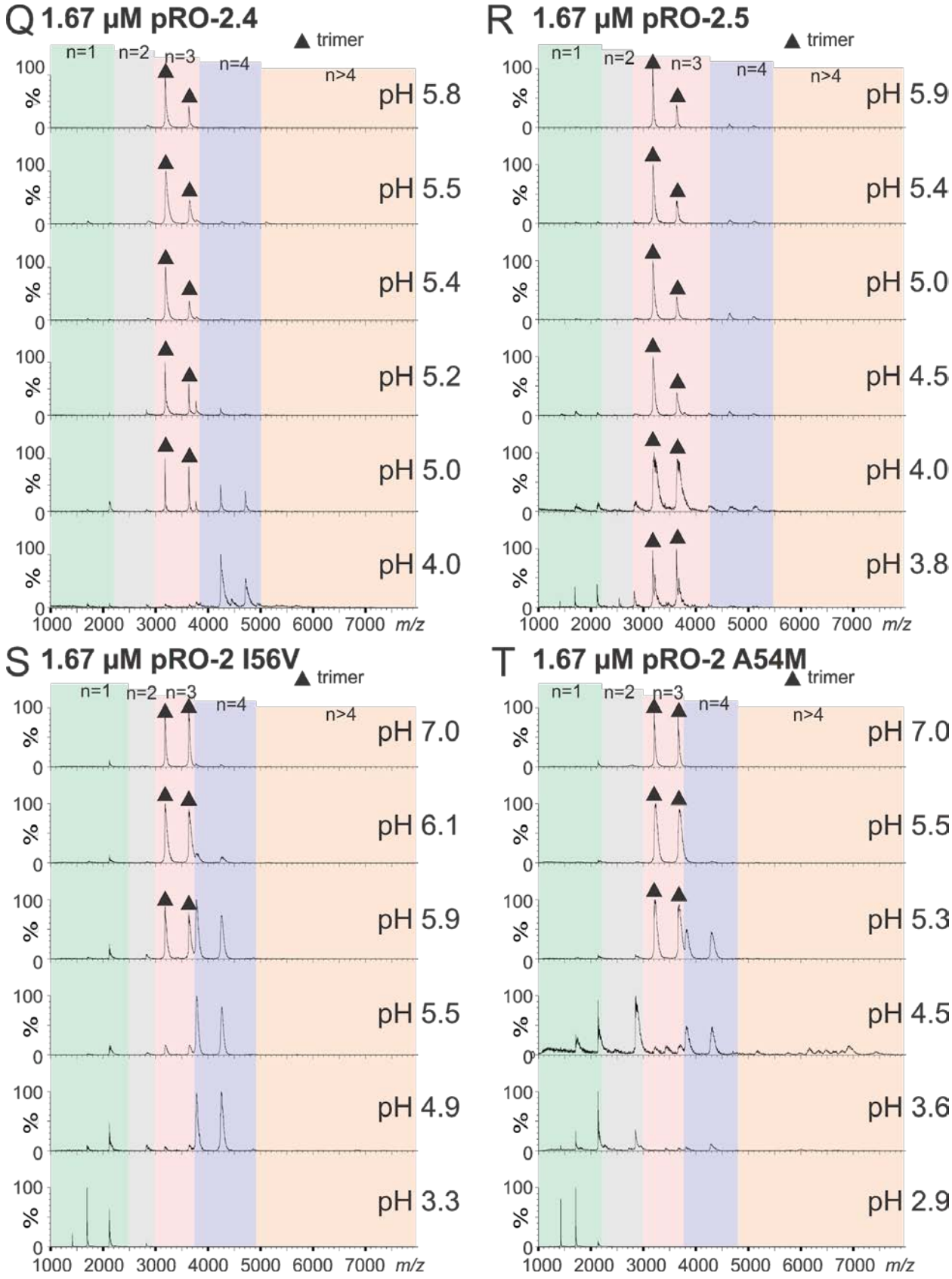
Q 1.67 µM pRO-2.4
R 1.67 µM pRO-2.5
S 1.67 µM pRO-2 I56V
T 1.67 µM pRO-2 A54M
trimer
n=1
n=2
n=3
n=4
n>4
pH 5.8
pH 5.5
pH 5.4
pH 5.2
pH 5.0
pH 4.0
pH 5.9
pH 5.4
pH 5.0
pH 4.5
pH 4.0
pH 3.8
pH 7.0
pH 6.1
pH 5.9
pH 5.5
pH 4.9
pH 3.3
pH 7.0
pH 5.5
pH 5.3
pH 4.5
pH 3.6
pH 2.9
100
%
0
1000 2000 3000 4000 5000 6000 7000 m/z

Fig. S14. pH-induced changes in oligomeric state as determined by native MS: Mass spectra are shown at the indicated pH to illustrate differences in dissociation pathways for the designs; the number of subunits in each observed oligomeric complex is denoted by n (*e.g.* n=3 indicates trimer, and n=1 indicates monomer). Trimers 2L6HC3_13 (**A**), pRO-2-noHis (**B**), and pRO-2.2 (**E**, **O**) show no significant pH response within pH ~7.0 to ~3.0. Trimers pRO-2 (**C**, **M**), pRO-2.1 (**D**, **N**), pRO-2.4 (**G**, **Q**), pRO-3 (**I**), pRO-3.1 (**J**), pRO-2 I56V (**S**) and pRO-2 A54M (**T**) disassemble via tetramer as intermediate, whereas pRO-2.5 (**H**, **R**) seems to directly dissociate into monomer at low pH. pRO-2.3 (**F**, **P**) forms multiple higher-order oligomers besides tetramer at low pH prior to dissociation into monomer. Dimers pRO-4 (**K**) and pRO-5 (**L**) predominantly directly dissociate into monomer at low pH. The occurrence of characteristic intermediates in pH-dependent dissociation of the designs was observed to be independent of concentration, although concentration does somewhat affect the relative percentages of the different intermediate states observed; concentrations are with respect to the initial oligomeric state at neutral pH (*e.g.* 5 µM pRO-2 indicates 5 µM of trimer species in the sample).

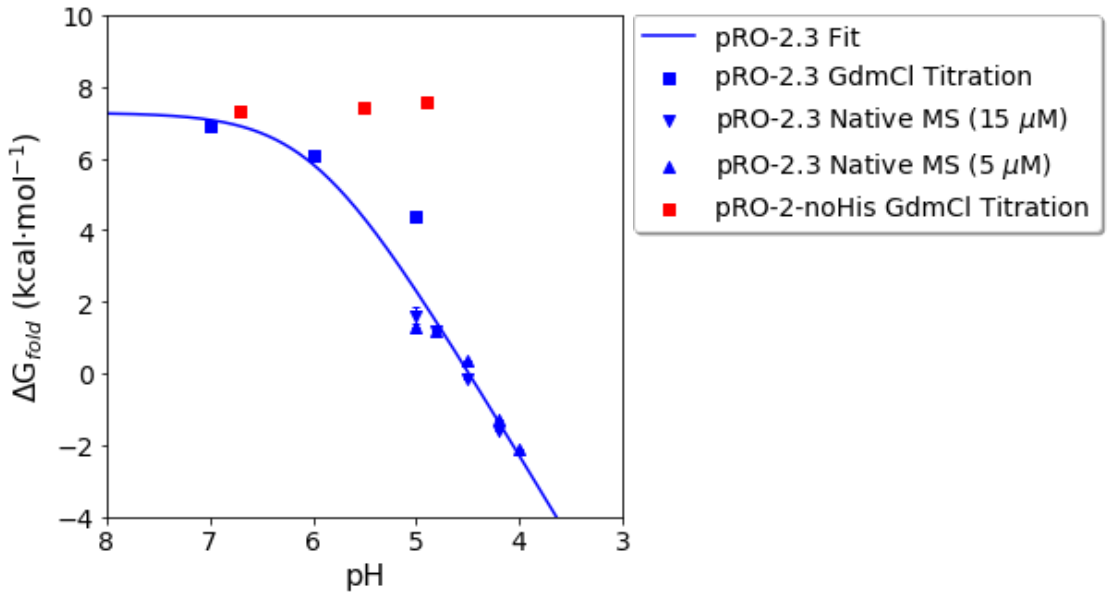

Fig. S15. ΔG_{fold} values fit to Equation S1 for pH-responsive design pRO-2.3 (blue) from guanidinium chloride (GdmCl) denaturation experiments in the folded regime (pH > ~4.5) (table S6) and the population fraction of trimer from native mass spectrometry (MS) experiments in the pH-unfolding transition region (pH 4.0-5.0) (obtained from fitting native MS data to Equation S7). ΔG_{fold} values for non-pH-responsive design pRO-2-noHis (red) from GdmCl denaturation experiments in the folded regime (table S6) are shown for comparison. Error bars represent the standard deviations of replicate native mass spectrometry experiments.

Supplementary Tables S1-S6

Table S1: Amino acid sequences of all designs tested. All constructs were cloned into pET21-NESG plasmid except for design pRO-1, which was cloned in pET28b. Heterodimers pRO-4 and pRO-5 were ordered as bicistronic constructs; DNA sequence containing stop codon, additional ribosome binding sequence, and second start codon is shown by the lower-case letters in parenthesis. Underlined regions are removed after hexahistidine tag cleavage. Bold positions indicate mutations/differences between a design variant and its parent design.

Design name	Amino acid sequences of designed proteins in this study
pRO-1	MGSSHHHHHHSSGLVPRGSHMGTLKEVLERLEEVLRRHREVAREHQRWAREHEQ WVRDDPNSAKWIAESTRWILETTDAISRTADVLAEAIRVLAESD
pRO-2	MGSHHHHHHGSGSENLYFQGSEYEIRKALEELKAATAELKRATASLRAITEELKK NPSEDALVEHNRAIVEHNAIIVEHNRIIAAVLELIVRAIK
pRO-2 H45N / H52N / H59N	MGSHHHHHHGSGSENLYFQGSEYEIRKALEELKAATAELKRATASLRAITEELKK NPSEDALVE**N**NRAIVE**N**NAIIVE**N**NRIIAAVLELIVRAIK
pRO-2-noHis	MGSHHHHHHGSGSENLYFQGSEYEIRKALEELKA**S**TAELKR**S**TASLRA**S**TEELKK NPSEDALVE**N**NR**L**IVE**N**NAIIVE**N**NRIIAAVLELIVRAIK
pRO-2.1	MGSHHHHHHGSGSENLYFQGSEYEIRKALEELKAA**L**AELKRATASLRAITEELKK NPSEDALVEHNRAIVEHNAIIVE**VL**RIIAAVLELIVRAIK
pRO-2.2	MGSHHHHHHGSGSENLYFQGSEYEIRKALEELKAA**L**AELKRATASLRAI**L**EELKK NPSEDA**I**VE**AI**RAIVEHNAIIVE**VL**RIIAAVLELIVRAIK
pRO-2.3	MGSHHHHHHGSGSENLYFQGSEYEIRKALEELKA**S**TAELKRATASLRAITEELKK NPSEDALVEHNRAIVEHNAIIVE**N**NRIIAAVLELIVRAIK
pRO-2.4	MGSHHHHHHGSGSENLYFQGSEYEIRKALEELKAATAELKRATASLRA**S**TEELKK NPSEDALVE**N**NR**L**IVEHNAIIVEHNRIIAAVLELIVRAIK
pRO-2.5	MGSHHHHHHGSGSENLYFQGSEYEIRKALEELKA**S**TAELKRATASLRA**S**TEELKK NPSEDALVE**N**NR**L**IVEHNAIIVE**N**NRIIAAVLELIVRAIK
pRO-2 I56V	MGSHHHHHHGSGSENLYFQGSEYEIRKALEELKAATAELKRATASLRAITEELKK NPSEDALVEHNRAIVEHNAI**V**VEHNRIIAAVLELIVRAIK
pRO-2 A54M	MGSHHHHHHGSGSENLYFQGSEYEIRKALEELKAATAELKRATASLRAITEELKK NPSEDALVEHNRAIVEHN**M**IIVEHNRIIAAVLELIVRAIK
pRO-2 I70N	MGSHHHHHHGSGSENLYFQGSEYEIRKALEELKAATAELKRATASLRAITEELKK NPSEDALVEHNRAIVEHNAIIVEHNRIIAAVLEL**N**VRAIK
pRO-3	MGSHHHHHHGSGSENLYFQGSEALYELEKALRELKKATAALERATAELKKNPSE DALVEHNRLIAAHNKIIAEVLRIIAKVLK
pRO-3.1	MGSHHHHHHGSGSENLYFQGSEALYELEKATRELKKATDELERATEELEKNPSED ALVEHNRLIAEHNKIIAEHNRIIAKVLK
pRO-4	MDEEDHLKKLKTHLEKLERHLKLLEDHAKKLEDILKERPEDSAVKESIDELRRSIE

	LVRESIEIFRQSVEEEE(**taa**gaaggagatatcatc**atg**)GSSHHHHHHSSGENLYFQGDVKELT KILDTLTKILETATKVIKDATKLLEEHRKSDKPDPRLIETHKKLVEEHETLVRQHKE LAEEHLKRTR
pRO-4 L23A / V130A	MDEEDHLKKLKTHLEKLERHLKLAEDHAKKLEDILKERPEDSAVKESIDELRRSIE LVRESIEIFRQSVEEEE(**taa**gaaggagatatcatc**atg**)GSSHHHHHHSSGENLYFQGDVKELT KILDTLTKILETATKVIKDATKLLEEHRKSDKPDPRLIETHKKLVEEHETLARQHKE LAEEHLKRTR
pRO-5	MTKEDILERQRKIIERAQEIHRRQQEILKEQEKIIRKPGSSEEAMKRSLKLIEESLRLL KELLELSEESAQLLYEQR(**taa**gaaggagatatcatc**atg**)GSSHHHHHHSSGENLYFQGTEKR LLEEAERAHREQKEIIKKAQELHKELTKIHQQSGSSEEAKKRALKISQEIRELSKRSL ELLREILYLSQEQK
pRO-2-GS	MGSHHHHHHGSGSENLYFQGSEYEIRKALEELKAATAELKRATASLRAITEELKK **GGSGSG**SEDALVEHNRAIVEHNAIIVEHNRIIAAVLELIVRAIK
pRO-2.3-GS	MGSHHHHHHGSGSENLYFQGSEYEIRKALEELKA**S**TAELKRATASLRAITEELKK **GGSGSG**SEDALVEHNRAIVEHNAIIVE**N**NRIIAAVLELIVRAIK

Table S2: X-ray crystallography data collection and refinement statistics.

	pRO-2.3 (6MSQ)	**pRO-2.5** (6MSR)
Wavelength	0.9999	1
Resolution range	43.79 - 1.28 (1.326 - 1.28)	28.7 - 1.55 (1.605 - 1.55)
Space group	P 63	C 1 2 1
Unit cell	50.5663 50.5663 130.753 90 90 120	57.618 33.281 114.455 90 99.557 90
Total reflections	429120 (15514)	142682 (14317)
Unique reflections	48463 (4882)	31393 (3139)
Multiplicity	8.8 (6.4)	4.5 (4.6)
Completeness (%)	99.8 (100.0)	95.36 (89.40)
Mean I/sigma(I)	7.83 (0.5)	9.97 (1.49)
Wilson B-factor	16.44	24.47
R-merge	0.117 (3.554)	0.07484 (1.027)
R-meas	0.125 (3.880)	0.08526 (1.164)
R-pim	0.042 (1.536)	0.04017 (0.5402)
CC1/2	0.998 (0.428)	0.995 (0.728)
CC*	1 (0.701)	0.999 (0.918)
Reflections used in refinement	48462 (2888)	31393 (2808)
Reflections used for R-free	1657 (115)	1407 (129)
R-work	0.1726 (0.5196)	0.2424 (0.3852)
R-free	0.1944 (0.5228)	0.2639 (0.3803)
CC(work)	0.961 (0.276)	0.954 (0.770)
CC(free)	0.965 (0.253)	0.966 (0.803)
Number of non-hydrogen atoms	1423	1916
macromolecules	1172	1755
solvent	251	161
Protein residues	152	228
RMS(bonds)	0.007	0.005
RMS(angles)	0.73	0.83
Ramachandran favored (%)	100.00	100.00
Ramachandran allowed (%)	0.00	0.00
Ramachandran outliers (%)	0.00	0.00
Rotamer outliers (%)	0.00	2.40
Clashscore	0.84	3.16
Average B-factor	26.70	43.57
macromolecules	24.47	43.33
solvent	37.08	46.19
Number of TLS groups		6

Statistics for the highest-resolution shell are shown in parentheses.

Table S3. Predicted and experimentally observed values for the cooperativity (k) and pH transition point of disassembly (pH_0). Values for $k_{observed}$ and $pH_{0\_observed}$ were obtained from fitting native mass spectrometry data (Figure 3D) to Equation S3: data was collected at a protein concentration of 5 μM or 1.67 μM (shown in parenthesis) with respect to the trimeric species. Predicted values for pH_0 were obtained from Equation S4, which relates Equations S2 and S3 to predict pH_0 as a function of n, m, and l; and $k_{predicted}$ can be approximated by $3m \cdot \ln(10)$, as described above. Hill coefficients were estimated from fitting native mass spectrometry data to Equation S5.

Design Name	n	m	l	$k_{predicted}$	$k_{observed}$	$pH_{0\_predicted}$	$pH_{0\_observed}$	Hill coefficient
pRO-2	6	3	0	20.72	4.81 (3.35)	5.37	5.50 (5.13)	2.09 (1.46)
pRO-2-noHis	6	0	3	0.0	not observed*	~0.0	not observed*	not observed*
pRO-2.1	7	2	0	13.82	14.69 (8.27)	4.42	3.74 (3.86)	6.37 (3.59)
pRO-2.2	8	1	0	6.91	not observed*	1.56	not observed*	not observed*
pRO-2.3	6	2	1	13.82	11.21 (8.71)	5.14	4.61 (4.42)	3.75 (3.78)
pRO-2.4	6	2	1	13.82	2.59 (3.56)	5.14	5.32 (4.91)	1.12 (1.55)
pRO-2.5	6	1	2	6.91	1.43 (1.19)	4.43	4.1 (3.45)	0.62 (0.52)
pRO-3	5	2	0	13.82	11.52 (5.79)	5.05	5.07 (4.87)	5.01 (2.51)
pRO-3.1	4	3	0	20.72	4.28 (3.77)	5.79	5.24 (5.77)	**
pRO-2 I56V	6	3	0	20.72	(3.65)	5.69	(5.83)	(1.59)
pRO-2 A54M	6	3	0	20.72	(3.60)	5.15	(4.97)	(1.56)

***not observed** indicates that dissociation was not observed within the experimentally-tested pH range (down to pH ~3.0).

**unable to obtain reliable estimates of Hill coefficient from native mass spectrometry data.

Table S4. SAXS data collection and analysis.

Design name	Concentration (mg ml^{-1})	$I(0)$ (cm^{-1}) [from $P(r)$]	R_g (Å) [from $P(r)$]	$I(0)$ (cm^{-1}) [from Guinier]	R_g (Å) [from Guinier]	D_{max} (Å)	Perod volume estimate (Å^3)	R_c	P_x
pRO-2	5.0	1570	21.66	1670	21.97	72	50287	14.2	3.4
pRO-2-noHis	3.8	1070	21.54	1090	21.36	70	46442	13.7	3.5

Table S5: Native mass spectrometry: expected and observed masses for proteins in this study. The deviation between observed and expected masses for pRO-4 is are due to salt-adducts, which are commonly observed under gentle MS conditions.

Design name	Oligomeric state at neutral pH	Expected mass (Da)	Determined mass (Da)
pRO-1	2	19087.01	19087+/-0 (+G)
pRO-2	3	25445.03	25444+/-0
pRO-2-NoHis	3	25381.70	25382+/-0
pRO-2.1	3	25364.33	25364+/-0
pRO-2.2	3	25199.48	25199+/-1
pRO-2.3	3	25423.92	25425+/-0
pRO-2.4	3	25423.92	25424+/-0
pRO-2.5	3	25402.81	25404+/-1
pRO-2 I56V	3	25402.95	25402+/-0
pRO-2 A54M	3	25625.39	25625+/-0
pRO-3	3	21309.69	21310+/-0
pRO-3.1	3	22047.57	22047+/-0
pRO-4	2	17534.82	17666+/-0(+1M)
pRO-5	2	18478.04	18347+/-0 (-1M)
pRO-2-GS	3	26018.46	26018+/-0
pRO-2.3-GS	3	25997.35	25997+/-0
2L6HC3_13	3	27384.89	27385+/-0

Table S6. Summary of guanidine denaturation experiments. Values for ΔG_{fold} and m_{GdmCl} for each design at different pH values were obtained by fitting guanidinium chloride concentration ([GdmCl]) to the mean residue ellipticity at 222 nm (MRE_{222nm}) circular dichroism data according to Equation S6 for guanidinium chloride titration experiments. C_m values are calculated according to $C_m = \Delta G_{fold} m_{GdmCl}$. Denaturation experiments in which a two-state unfolding transition was not observed are not shown, and values omitted where $C_m > 6$ due to incomplete protein denaturation for the guanidine concentrations tested.

Design Name	*n*	*m*	*l*	pH	Buffer	ΔG_{fold} (kcal·mol^{-1})	m_{GdmCl} (kcal·L·mol^{-2})	C_m (mol·L^{-1})
pRO-2	6	3	0	7.4	PBS	7.71	2.46	3.14
pRO-2	6	3	0	6.7	Na_2HPO_4-Citrate	7.00	2.23	3.13
pRO-2	6	3	0	6.7	Na_2HPO_4-Citrate	7.00	2.23	3.13
pRO-2	6	3	0	6.7	Na_2HPO_4-Citrate	7.00	2.23	3.13
pRO-2	6	3	0	5.5	Na_2HPO_4-Citrate	6.09	2.65	2.30
pRO-2	6	3	0	5.5	Na_2HPO_4-Citrate	6.09	2.65	2.30
pRO-2 A54M	6	3	0	5.5	Na_2HPO_4-Citrate	7.58	2.75	2.76
pRO-2 A54M	6	3	0	4.9	Na_2HPO_4-Citrate	5.03	2.11	2.38
pRO-2 I56V	6	3	0	7.4	PBS	7.16	3.04	2.36
pRO-2 I56V	6	3	0	6.7	Na_2HPO_4-Citrate	7.33	2.91	2.52
pRO-2 I56V	6	3	0	5.5	Na_2HPO_4-Citrate	6.94	2.79	2.48
pRO-2-noHis	6	0	3	7.4	PBS	7.16	3.04	2.36
pRO-2-noHis	6	0	3	6.7	Na_2HPO_4-Citrate	7.32	2.91	2.52
pRO-2-noHis	6	0	3	5.5	Na_2HPO_4-Citrate	7.43	2.77	2.68
pRO-2-noHis	6	0	3	4.9	Na_2HPO_4-Citrate	7.59	2.68	2.83
pRO-2.1	7	2	0	7.4	PBS	-	-	> 6
pRO-2.1	7	2	0	7.4	PBS	-	-	> 6
pRO-2.1	7	2	0	7.4	PBS	-	-	> 6
pRO-2.3	6	2	1	7.4	PBS	8.38	3.88	2.16
pRO-2.3	6	2	1	7.0	Na_2HPO_4-Citrate	6.90	3.01	2.29
pRO-2.3	6	2	1	6.0	Na_2HPO_4-Citrate	6.06	3.24	1.87
pRO-2.3	6	2	1	5.0	Na_2HPO_4-Citrate	4.36	2.69	1.62

pRO-2.4	6	2	1	7.4	PBS	7.04	2.98	2.36
pRO-2.4	6	2	1	7.4	PBS	7.22	3.06	2.36
pRO-2.4	6	2	1	6.7	Na_2HPO_4-Citrate	7.60	2.83	2.68
pRO-2.5	6	1	2	7.4	PBS	7.08	3.91	1.81
pRO-2.5	6	1	2	6.7	Na_2HPO_4-Citrate	6.77	3.37	2.00

References and Notes

1. C. B. Anfinsen, Principles that govern the folding of protein chains. *Science* **181**, 223–230 (1973). doi:10.1126/science.181.4096.223 Medline

2. P.-S. Huang, S. E. Boyken, D. Baker, The coming of age of de novo protein design. *Nature* **537**, 320–327 (2016). doi:10.1038/nature19946 Medline

3. G. J. Rocklin, T. M. Chidyausiku, I. Goreshnik, A. Ford, S. Houliston, A. Lemak, L. Carter, R. Ravichandran, V. K. Mulligan, A. Chevalier, C. H. Arrowsmith, D. Baker, Global analysis of protein folding using massively parallel design, synthesis, and testing. *Science* **357**, 168–175 (2017). doi:10.1126/science.aan0693 Medline

4. C. M. Carr, P. S. Kim, A spring-loaded mechanism for the conformational change of influenza hemagglutinin. *Cell* **73**, 823–832 (1993). doi:10.1016/0092-8674(93)90260-W Medline

5. J. M. White, S. E. Delos, M. Brecher, K. Schornberg, Structures and mechanisms of viral membrane fusion proteins: Multiple variations on a common theme. *Crit. Rev. Biochem. Mol. Biol.* **43**, 189–219 (2008). doi:10.1080/10409230802058320 Medline

6. C. M. Mair, K. Ludwig, A. Herrmann, C. Sieben, Receptor binding and pH stability - how influenza A virus hemagglutinin affects host-specific virus infection. *Biochem. Biophys. Acta* **1838**, 1153–1168 (2014). doi:10.1016/j.bbamem.2013.10.004 Medline

7. M. L. Murtaugh, S. W. Fanning, T. M. Sharma, A. M. Terry, J. R. Horn, A combinatorial histidine scanning library approach to engineer highly pH-dependent protein switches. *Protein Sci.* **20**, 1619–1631 (2011). doi:10.1002/pro.696 Medline

8. E.-M. Strauch, S. J. Fleishman, D. Baker, Computational design of a pH-sensitive IgG binding protein. *Proc. Natl. Acad. Sci. U.S.A.* **111**, 675–680 (2014). doi:10.1073/pnas.1313605111 Medline

9. N. Gera, A. B. Hill, D. P. White, R. G. Carbonell, B. M. Rao, Design of pH sensitive binding proteins from the hyperthermophilic Sso7d scaffold. *PLOS ONE* **7**, e48928 (2012). doi:10.1371/journal.pone.0048928 Medline

10. M. Dalmau, S. Lim, S.-W. Wang, pH-triggered disassembly in a caged protein complex. *Biomacromolecules* **10**, 3199–3206 (2009). doi:10.1021/bm900674v Medline

11. T. Igawa, S. Ishii, T. Tachibana, A. Maeda, Y. Higuchi, S. Shimaoka, C. Moriyama, T. Watanabe, R. Takubo, Y. Doi, T. Wakabayashi, A. Hayasaka, S. Kadono, T. Miyazaki, K. Haraya, Y. Sekimori, T. Kojima, Y. Nabuchi, Y. Aso, Y. Kawabe, K. Hattori, Antibody recycling by engineered pH-dependent antigen binding improves the duration of antigen neutralization. *Nat. Biotechnol.* **28**, 1203–1207 (2010). doi:10.1038/nbt.1691 Medline

12. K. Wada, T. Mizuno, J. Oku, T. Tanaka, pH-induced conformational change in an alpha-helical coiled-coil is controlled by His residues in the hydrophobic core. *Protein Pept. Lett.* **10**, 27–33 (2003). doi:10.2174/0929866033408354 Medline

13. R. Lizatović, O. Aurelius, O. Stenström, T. Drakenberg, M. Akke, D. T. Logan, I. André, A De Novo Designed Coiled-Coil Peptide with a Reversible pH-Induced Oligomerization Switch. *Structure* **24**, 946–955 (2016). doi:10.1016/j.str.2016.03.027 Medline

14. K. Pagel, S. C. Wagner, K. Samedov, H. von Berlepsch, C. Böttcher, B. Koksch, Random coils, β-sheet ribbons, and α-helical fibers: One peptide adopting three different secondary structures at will. *J. Am. Chem. Soc.* **128**, 2196–2197 (2006). doi:10.1021/ja057450h Medline

15. C. Minelli, J. X. Liew, M. Muthu, H. Andresen, Coiled coil peptide -functionalized surfaces for reversible molecular binding. *Soft Matter* **9**, 5119–5124 (2013). doi:10.1039/c3sm50379h

16. J. Aupič, F. Lapenta, R. Jerala, SwitCCh: Metal-site design for controlling the assembly of a coiled-coil homodimer. *ChemBioChem* **19**, 2453–2457 (2018). 10.1002/cbic.201800578 Medline

17. Y. Zhang, R. Bartz, G. Grigoryan, M. Bryant, J. Aaronson, S. Beck, N. Innocent, L. Klein, W. Procopio, T. Tucker, V. Jadhav, D. M. Tellers, W. F. DeGrado, Computational design and experimental characterization of peptides intended for pH-dependent membrane insertion and pore formation. *ACS Chem. Biol.* **10**, 1082–1093 (2015). doi:10.1021/cb500759p Medline

18. F. H. C. Crick, The Fourier transform of a coiled-coil. *Acta Crystallogr.* **6**, 685–689 (1953). doi:10.1107/S0365110X53001952

19. G. Grigoryan, W. F. Degrado, Probing designability via a generalized model of helical bundle geometry. *J. Mol. Biol.* **405**, 1079–1100 (2011). doi:10.1016/j.jmb.2010.08.058 Medline

20. S. E. Boyken, Z. Chen, B. Groves, R. A. Langan, G. Oberdorfer, A. Ford, J. M. Gilmore, C. Xu, F. DiMaio, J. H. Pereira, B. Sankaran, G. Seelig, P. H. Zwart, D. Baker, De novo design of protein homo-oligomers with modular hydrogen-bond network-mediated specificity. *Science* **352**, 680–687 (2016). doi:10.1126/science.aad8865 Medline

21. B. Kuhlman, D. Baker, Native protein sequences are close to optimal for their structures. *Proc. Natl. Acad. Sci. U.S.A.* **97**, 10383–10388 (2000). doi:10.1073/pnas.97.19.10383 Medline

22. A. Leaver-Fay *et al*., in *Methods in Enzymology*, M. L. Johnson, L. Brand, Eds. (Academic Press, 2011), vol. 487, pp. 545–574.

23. P.-S. Huang, G. Oberdorfer, C. Xu, X. Y. Pei, B. L. Nannenga, J. M. Rogers, F. DiMaio, T. Gonen, B. Luisi, D. Baker, High thermodynamic stability of parametrically designed helical bundles. *Science* **346**, 481–485 (2014). doi:10.1126/science.1257481 Medline

24. S. Mehmood, T. M. Allison, C. V. Robinson, Mass spectrometry of protein complexes: From origins to applications. *Annu. Rev. Phys. Chem.* **66**, 453–474 (2015). doi:10.1146/annurev-physchem-040214-121732 Medline

25. E. Boeri Erba, K. Barylyuk, Y. Yang, R. Zenobi, Quantifying protein-protein interactions within noncovalent complexes using electrospray ionization mass spectrometry. *Anal. Chem.* **83**, 9251–9259 (2011). doi:10.1021/ac201576e Medline

26. N. Leloup, P. Lössl, D. H. Meijer, M. Brennich, A. J. R. Heck, D. M. E. Thies-Weesie, B. J. C. Janssen, Low pH-induced conformational change and dimerization of sortilin triggers endocytosed ligand release. *Nat. Commun.* **8**, 1708 (2017). doi:10.1038/s41467-017-

01485-5 Medline

27. Y.-B. Hu, E. B. Dammer, R.-J. Ren, G. Wang, The endosomal-lysosomal system: From acidification and cargo sorting to neurodegeneration. *Transl. Neurodegener.* **4**, 18 (2015). doi:10.1186/s40035-015-0041-1 Medline

28. M. Grabe, G. Oster, Regulation of organelle acidity. *J. Gen. Physiol.* **117**, 329–344 (2001). doi:10.1085/jgp.117.4.329 Medline

29. K. N. Dyer, M. Hammel, R. P. Rambo, S. E. Tsutakawa, I. Rodic, S. Classen, J. A. Tainer, G. L. Hura, High-throughput SAXS for the characterization of biomolecules in solution: A practical approach. *Methods Mol. Biol.* **1091**, 245–258 (2014). doi:10.1007/978-1-62703-691-7_18 Medline

30. S. Classen, G. L. Hura, J. M. Holton, R. P. Rambo, I. Rodic, P. J. McGuire, K. Dyer, M. Hammel, G. Meigs, K. A. Frankel, J. A. Tainer, Implementation and performance of SIBYLS: A dual endstation small-angle X-ray scattering and macromolecular crystallography beamline at the Advanced Light Source. *J. Appl. Crystallogr.* **46**, 1–13 (2013). doi:10.1107/S0021889812048698 Medline

31. E. Eiríksdóttir, K. Konate, U. Langel, G. Divita, S. Deshayes, Secondary structure of cell-penetrating peptides controls membrane interaction and insertion. *Biochim. Biophys. Acta* **1798**, 1119–1128 (2010). doi:10.1016/j.bbamem.2010.03.005 Medline

32. L. Gui, K. K. Lee, in *Influenza Virus: Methods and Protocols*, Y. Yamauchi, Ed. (Springer New York, New York, NY, 2018), pp. 261–279.

33. C. S. Pillay, E. Elliott, C. Dennison, Endolysosomal proteolysis and its regulation. *Biochem. J.* **363**, 417–429 (2002). doi:10.1042/bj3630417 Medline

34. M. Li, Y. Tao, Y. Shu, J. R. LaRochelle, A. Steinauer, D. Thompson, A. Schepartz, Z.-Y. Chen, D. R. Liu, Discovery and characterization of a peptide that enhances endosomal escape of delivered proteins in vitro and in vivo. *J. Am. Chem. Soc.* **137**, 14084–14093 (2015). doi:10.1021/jacs.5b05694 Medline

35. M. S. Lawrence, K. J. Phillips, D. R. Liu, Supercharging proteins can impart unusual resilience. *J. Am. Chem. Soc.* **129**, 10110–10112 (2007). doi:10.1021/ja071641y Medline

36. J. Monod, J. Wyman, J.-P. Changeux, in *Selected Papers in Molecular Biology by Jacques Monod*, A. Lwoff, A. Ullmann, Eds. (Academic Press, 1978), pp. 593–623.

37. E. L. Snyder, S. F. Dowdy, Cell penetrating peptides in drug delivery. *Pharm. Res.* **21**, 389–393 (2004). doi:10.1023/B:PHAM.0000019289.61978.f5 Medline

38. Y. S. Choi, M. Y. Lee, A. E. David, Y. S. Park, Nanoparticles for gene delivery: Therapeutic and toxic effects. *Mol. Cell. Toxicol.* **10**, 1–8 (2014). doi:10.1007/s13273-014-0001-3

39. A. S. Yang, B. Honig, On the pH dependence of protein stability. *J. Mol. Biol.* **231**, 459–474 (1993). doi:10.1006/jmbi.1993.1294 Medline

40. K. Dutta, A. Alexandrov, H. Huang, S. M. Pascal, pH-induced folding of an apoptotic coiled coil. *Protein Sci.* **10**, 2531–2540 (2001). doi:10.1110/ps.28801 Medline

41. V. Martins de Oliveira, V. Godoi Contessoto, F. Bruno da Silva, D. L. Zago Caetano, S. Jurado de Carvalho, V. B. Pereira Leite, Effects of pH and Salt Concentration on Stability

of a Protein G Variant Using Coarse-Grained Models. *Biophys. J.* **114**, 65–75 (2018). doi:10.1016/j.bpj.2017.11.012 Medline

42. F. W. Studier, Protein production by auto-induction in high density shaking cultures. *Protein Expr. Purif.* **41**, 207–234 (2005). doi:10.1016/j.pep.2005.01.016 Medline

43. M. Zhou, C. Huang, V. H. Wysocki, Surface-induced dissociation of ion mobility-separated noncovalent complexes in a quadrupole/time-of-flight mass spectrometer. *Anal. Chem.* **84**, 6016–6023 (2012). doi:10.1021/ac300810u Medline

44. R. P. Rambo, J. A. Tainer, Characterizing flexible and intrinsically unstructured biological macromolecules by SAS using the Porod-Debye law. *Biopolymers* **95**, 559–571 (2011). doi:10.1002/bip.21638 Medline

45. D. Schneidman-Duhovny, M. Hammel, A. Sali, FoXS: A web server for rapid computation and fitting of SAXS profiles. *Nucleic Acids Res.* **38** (Web Server), W540–W544 (2010). doi:10.1093/nar/gkq461 Medline

46. D. Schneidman-Duhovny, M. Hammel, J. A. Tainer, A. Sali, Accurate SAXS profile computation and its assessment by contrast variation experiments. *Biophys. J.* **105**, 962–974 (2013). doi:10.1016/j.bpj.2013.07.020 Medline

47. W. Kabsch, XDS. *Acta Crystallogr. D Biol. Crystallogr.* **66**, 125–132 (2010). doi:10.1107/S0907444909047337 Medline

48. A. J. McCoy, R. W. Grosse-Kunstleve, P. D. Adams, M. D. Winn, L. C. Storoni, R. J. Read, Phaser crystallographic software. *J. Appl. Crystallogr.* **40**, 658–674 (2007). doi:10.1107/S0021889807021206 Medline

49. P. D. Adams, P. V. Afonine, G. Bunkóczi, V. B. Chen, I. W. Davis, N. Echols, J. J. Headd, L.-W. Hung, G. J. Kapral, R. W. Grosse-Kunstleve, A. J. McCoy, N. W. Moriarty, R. Oeffner, R. J. Read, D. C. Richardson, J. S. Richardson, T. C. Terwilliger, P. H. Zwart, PHENIX: A comprehensive Python-based system for macromolecular structure solution. *Acta Crystallogr. D Biol. Crystallogr.* **66**, 213–221 (2010). doi:10.1107/S0907444909052925 Medline

50. T. C. Terwilliger, R. W. Grosse-Kunstleve, P. V. Afonine, N. W. Moriarty, P. H. Zwart, L.-W. Hung, R. J. Read, P. D. Adams, Iterative model building, structure refinement and density modification with the PHENIX AutoBuild wizard. *Acta Crystallogr. D Biol. Crystallogr.* **64**, 61–69 (2008). doi:10.1107/S090744490705024X Medline

51. P. Emsley, K. Cowtan, Coot: Model-building tools for molecular graphics. *Acta Crystallogr. D Biol. Crystallogr.* **60**, 2126–2132 (2004). doi:10.1107/S0907444904019158 Medline

52. I. W. Davis, A. Leaver-Fay, V. B. Chen, J. N. Block, G. J. Kapral, X. Wang, L. W. Murray, W. B. Arendall 3rd, J. Snoeyink, J. S. Richardson, D. C. Richardson, MolProbity: All-atom contacts and structure validation for proteins and nucleic acids. *Nucleic Acids Res.* **35** (Web Server), W375–W383 (2007). doi:10.1093/nar/gkm216 Medline

53. C. Suloway, J. Pulokas, D. Fellmann, A. Cheng, F. Guerra, J. Quispe, S. Stagg, C. S. Potter, B. Carragher, Automated molecular microscopy: The new Leginon system. *J. Struct. Biol.* **151**, 41–60 (2005). doi:10.1016/j.jsb.2005.03.010 Medline

54. S. Q. Zheng, E. Palovcak, J.-P. Armache, K. A. Verba, Y. Cheng, D. A. Agard, MotionCor2:

Anisotropic correction of beam-induced motion for improved cryo-electron microscopy. *Nat. Methods* **14**, 331–332 (2017). doi:10.1038/nmeth.4193 Medline

55. D. N. Mastronarde, S. R. Held, Automated tilt series alignment and tomographic reconstruction in IMOD. *J. Struct. Biol.* **197**, 102–113 (2017). doi:10.1016/j.jsb.2016.07.011 Medline

56. A. Rohou, N. Grigorieff, CTFFIND4: Fast and accurate defocus estimation from electron micrographs. *J. Struct. Biol.* **192**, 216–221 (2015). doi:10.1016/j.jsb.2015.08.008 Medline

57. C. A. Schneider, W. S. Rasband, K. W. Eliceiri, NIH Image to ImageJ: 25 years of image analysis. *Nat. Methods* **9**, 671–675 (2012). doi:10.1038/nmeth.2089 Medline

58. Z. Diwu, C. S. Chen, C. L. Zhang, D. H. Klaubert, R. P. Haugland, in *Abstracts of Papers of the American Chemical Society* (American Chemical Society, 1999), vol. 218, pp. U27–U27.

59. L. L. C. Schrödinger, The PyMOL molecular graphics system, version 1.7. 6.6 (2015).

60. E. Jones, T. Oliphant, P. Peterson, {SciPy}: Open source scientific tools for {Python} (2001–); www.scipy.org.

61. F. Busch, Z. L. VanAernum, Y. Ju, J. Yan, J. D. Gilbert, R. S. Quintyn, M. Bern, V. H. Wysocki, Localization of protein complex bound ligands by surface-induced dissociation high-resolution mass spectrometry. *Anal. Chem.* **90**, 12796–12801 (2018). doi:10.1021/acs.analchem.8b03263 Medline